Assessing Chemical and Mineralogical Properties of the Alpine Slab Based on Field Analogs and Ambient Noise Tomography

Manon Sonnet, Loïc Labrousse, Jerôme Bascou, Alexis Plunder, Ahmed Nouibat, Anne Paul

Geochemistry, Geophysics, Geosystems®

AGU ADVANCING EARTH AND SPACE SCIENCES

RESEARCH ARTICLE
10.1029/2022GC010784

Assessing Chemical and Mineralogical Properties of the Alpine Slab Based on Field Analogs and Ambient Noise Tomography

M. Sonnet[1], L. Labrousse[1], J. Bascou[2], A. Plunder[3], A. Nouibat[4], and A. Paul[4]

[1]ISTeP, UMR 7193, CNRS, Sorbonne Université, Paris, France, [2]LGL-TPE UMR5276, CNRS, Université Jean Monnet, Saint-Etienne, France, [3]BRGM, Orléans, France, [4]IRD, UGE, ISTerre, CNRS, Université Grenoble Alpes, Université Savoie Mont Blanc, Grenoble, France

Key Points:

- The lower crustal top of the European Alpine slab is mostly composed of felsic to intermediate rocks
- The transformation of hydrated rocks into HP granulites along a collision gradient reproduces the slab tomographic velocity increase at 30 km
- The often-supposed eclogitization produces velocities that are significantly higher than the crustal top of the European Alpine slab

Supporting Information:

Supporting Information may be found in the online version of this article.

Correspondence to:

M. Sonnet,
manon.sonnet@sorbonne-universite.fr

Citation:

Sonnet, M., Labrousse, L., Bascou, J., Plunder, A., Nouibat, A., & Paul, A. (2023). Assessing chemical and mineralogical properties of the Alpine slab based on field analogs and ambient noise tomography. *Geochemistry, Geophysics, Geosystems*, *24*, e2022GC010784. https://doi.org/10.1029/2022GC010784

Received 21 NOV 2022
Accepted 4 AUG 2023

Abstract Recent geophysical campaigns in the Alps produce images with seismic property variations along the slab of sufficiently fine resolution to be interpreted as rock transformations. Since the reacting European lower crust is presumed responsible for the variations of velocities at the top of the Alpine slab, we sampled local analogs of the lower crustal lithologies in the field and modeled the evolution of equilibrium seismic properties during burial, along possible pressure-temperature paths for the crustal portion of the slab. The results are then compared to the range of the *S*-wave velocities obtained from the *S*-wave velocity tomography model along the CIFALPS transect. The velocity increase from 25 to 45 km within the slab, in the tomographic model is best reproduced by the transformation of specific lithologies in the high-pressure granulite facies along a collisional gradient (30°C/km). Although the crust is certainly not completely homogeneous, the best candidates for the rocks that make up the top of the Alpine dip crustal panel are a kinzigite from Monte San Petrone, a gneiss from the Insubric line, and blueschist mylonite from Canavese. While they may not represent the entirety of the crust, they are sufficient to explain the tomographic velocity of the Alpine slab. A lateral lithological contrast inherited from the Variscan orogeny is not required. Eclogitization, suggested as the first-order transformation in convergence zones, could be a second-order transformation in collisional wedges. These results also imply a partially re-equilibrated thermal gradient, consistent with the Alpine thermal state data at depth.

Plain Language Summary Tomography, that is, imaging of deep geological structures based on seismic wave travel to time anomalies, is now so sensitive that it allows us to see changes in the properties of rocks buried at depth beneath mountain belts. In the Alps, the European plate is imaged down to 80 km and shows a sharp velocity increase close to 30 km depth. By calculating the bulk seismic wave velocities on exhumed analogs sampled throughout the Western Alps, the present study proposes to interpret the velocity jump as the consequence of the transformation of the European lower crust from amphibolite to granulite (the high-temperature metamorphic rocks produced during a collision) rather than the usually admitted transformation to eclogite (the higher pressure metamorphic rocks produced during subduction). This has implications regarding the present-day thermal structure of the Alps: the Western Alps are not a frozen subduction zone but a collision zone exposing subduction-related rocks and structures at the surface only.

1. Introduction

These last years the resolution and accuracy of geophysical images has improved, especially with the development of high-resolution large-scale projects in Europe such as AlpArray (with over 600 broadband stations spacing at less than 52 km, Heténi et al., 2018) or IberArray (with 130 broadband, Chevrot et al., 2014). They have produced detailed images showing lateral variations of seismic properties in wedges and beneath, that can be interpreted as variations of petrophysical properties, resulting from crustal and mantle deformation and/or metamorphism (Rondenay et al., 2008).

These lithology transformations have been recognized in several orogens (e.g., Heténi et al., 2018; Solarino et al., 2018; Zhang et al., 2014; Zhao et al., 2015). In the Himalayas, the seismic signature of the upper plate Moho in the receiver functions varies with the back-azimuth (J. L. Nábělek et al., 2005). This variation is interpreted as the evidence of a 10-km-thick anisotropic mica-bearing shear zone at the top of the under-plated Indian lower crust (LC) (J. Nábělek et al., 2009; Schulte-Pelkum et al., 2005; Zhang et al., 2014). Reaction kinetics have also been involved to explain deeper features. In the Himalayas, the comparison between density models and the

gravimetric data reveals that eclogitization of the Indian LC is delayed until the first dehydration reactions of the underlying mantle occur (Hetényi et al., 2021). These interpretations are not limited to large active convergent plate boundaries. In the Alps, current studies (Hetényi et al., 2018; Paul et al., 2021; Zhao et al., 2015) provide geophysical images of sufficiently high resolution to allow this same effort of interpretation (25 × 25 × 15 km for the V_p crustal structure, Diehl et al. (2009), or up to 15 × 15 × ~10 km, Solarino et al., 2018). In the Alps, the metamorphic transitions (e.g., blueschist to eclogite) are likely to be imaged by tomography because they occur as sharp to tens of kilometer-wide boundaries (e.g., the LT to the HT blueschist-facies transition in the Schistes Lustrés (SL) unit, Herviou et al., 2022).

The interpretation of these images and the determination of the rocks composing the crustal top of the Alpine panel require independent knowledge of the seismic velocities of the rocks potentially involved. Several world-wide databases of crustal rock seismic properties exist in the literature (e.g., Barruol & Mainprice, 1993; Lloyd et al., 2011; Rudnick & Fountain, 1995; Rudnick & Gao, 2003) and were recently used in the Alps (Malusà et al., 2021). However, the exact position of metamorphic transitions and associated velocity contrasts strongly depends on the chemical composition of rocks (e.g., Almqvist & Mainprice, 2017). The use of generic databases is hence an oversimplification that only gives first-order insights. Therefore, we need studies based on local analogs to refine our interpretations. To this end, it is crucial to build a regional catalog of quantified seismic properties, considering chemistry, pressure, temperature and metamorphic equilibration. The existence of such a catalog would be a precious tool to detect and identify the reaction fronts and infer the most probable lithologies constituting the crustal top of the Alpine slab at depth.

Initial interpretations of the NRP-20 WEST and ECORS CROP profiles proposed a duplex of LC beneath the internal Alps (Schmid & Kissling, 2000). The reinterpretation of the same transects in the light of new tomography results (Diehl et al., 2009), did not confirm such a duplex (Schmid et al., 2017). Thus, although this idea is not new (Marchant & Stampfli, 1997), the most recent interpretations consider that the European LC does not significantly participate in the crustal wedge formation and must therefore remain part of the down-going slab. Furthermore, balanced cross-sections through the Western Alps indicate a shortening of up to 66 km (Bellahsen et al., 2014). This shortening is consistent with a collision wedge composed mostly of upper crust. Finally, there is no evidence of a continuous unit derived from the European LC at the surface (Schmid et al., 2004), such as the Sesia Zone (SZ) for the Adriatic plate. Hence, the European LC is probably responsible for the strong visible wave conversions along the slab (e.g., Nouibat et al., 2022; Zhao et al., 2015). The presence of a large body of serpentinites in the subduction channel, metasomatized mantle peridotites and eclogitized LC have also been suggested in the interpretation of CIFALPS seismic images (Malusà et al., 2021; Zhao et al., 2020). A way to elaborate on this hypothesis of a LC component at the top of the subducted slab is to find disseminated outcrops of analogs of the LC in the field and model the evolution of their seismic properties during burial and metamorphic equilibrations. "Lower crust" is here understood in the sense of "lower crustal level" and not in the geochemical sense as in most global reviews of crustal composition (Lloyd et al., 2011; Rudnick & Fountain, 1995; Rudnick & Gao, 2003).

This study aims to critically assess the Alpine rocks as local analogs of crustal units of the subducted Alpine panel. The evolution of seismic properties of equilibrium rocks during burial, that is, along possible P-T trajectories for the slab, is predictably based on the evolution of its mineralogical assemblage and the thermoelastic parameters of each mineral (e.g., Almqvist & Mainprice, 2017). This provides the evolution of the isotropic component of the velocity tensor with depth. The obtained results are then compared to the seismic *S*-wave velocities from the tomographic model of Nouibat et al. (2022), along the CIFALPS profile, for which not only the V_s values but also their uncertainties are available. We discuss the results with emphasis on the interpretation of the velocity increase before 50 km depth within the crustal top of the slab as due to the presence of felsic to intermediate subject to progressive granulite-facies imprint. The implications for the evolution of the Alpine thermal state since the end of subduction are also discussed.

2. Seismic Velocities of the Alpine Slab Along the CIFALPS Transect

Along the CIFALPS transects, imaged at a resolution of 7 × 5–10 km in the horizontal direction and 0.2 km in the vertical direction (Paul et al., 2022; Zhao et al., 2015), the top of the European dipping slab appears connected to the European LC in *P*-wave to *S*-wave conversion models. Along the same transect, tomographic models, whose data are independent of the receiver functions, also show the same, in (a) *P*-wave tomography modeling, with

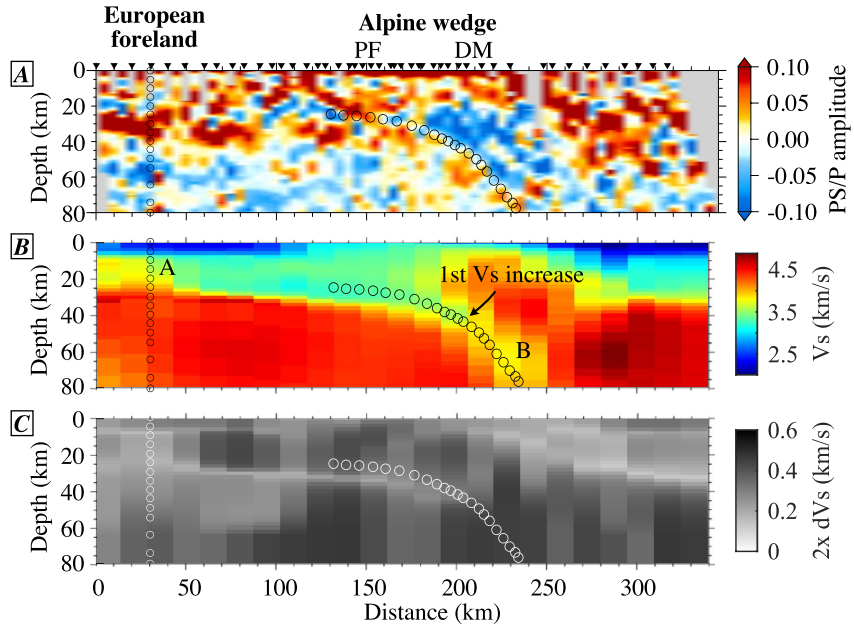

Figure 1. Location of representative depth velocity profile on CIFALPS transect (a) CCP receiver-function stack, (b) *S*-wave velocity tomography (data Nouibat et al., 2022) and (c) the associated uncertainties, for (a) the European plate at the front of the mountain belt and (b) the Alpine slab beneath the mountain range. Abbreviations: DM: Dora Maira, PF: Penninic Front.

a horizontal resolution of 20 km and a vertical resolution of 2–3 km (Solarino et al., 2018), and in (b) *S*-wave tomography model from ambient noise, with a horizontal resolution of 15 km and a vertical resolution of 1–4 km in the crust to 5–10 km in the mantle (Nouibat et al., 2022). Moreover, for the first time, this latter *S*-wave tomography model provides not only the velocities but also the uncertainties (from 0.15 to 0.20 km/s) associated with the group velocities, allowing critical geological interpretations. It is indeed possible to assess whether velocity variations resulting from rock transformations during burial lay within the model uncertainty or not. For this purpose, in the *S*-wave ambient noise tomography model (Figure 1; Nouibat et al., 2022), *S*-wave velocity curves as a function of depth are extracted along the CIFALPS transect from 2 areas: (area A) at the front of the mountain belt and in the foreland (Figures 1 and 2), as a representative of the European plate, and (area B) within the mountain belt, along the plunging slab defined based on receiver-function analyses (Figures 1 and 2).

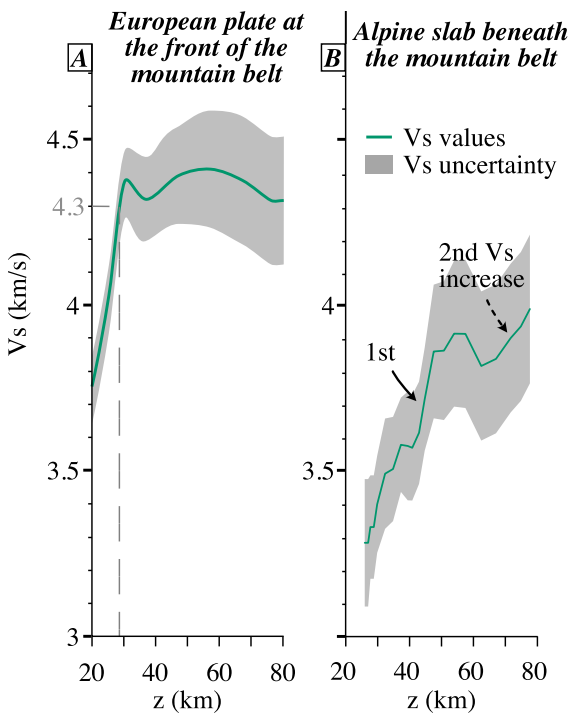

Figure 2. *S*-wave velocity profiles as a function of depth, in the European plate (a) and along the Alpine slab (b), extracted from the tomographic CIFALPS transect (Figure 1). The geophysical Moho corresponds to the velocity contour 4.3 km/s, selected by Nouibat et al. (2022) as the best Moho proxy for European crust out of the Alpine wedge.

The profile of the European plate corresponds to the data 15 km from the western end of the transect. Consideration of the probabilistic uncertainty of the *S*-wave tomographic model for each pixel allows to obtain ranges of possible seismic velocities for different domains across the chain. The uncertainty profile (Figure 1c) shows that the resolution is highest at velocity contrasts, such as the European Moho, which correspond to a standard error close to 2% (Figure 1c). Within the dipping panel, the velocity contrasts shallower than 50 km are better constrained than those deeper (4% vs. 6 or 7%, Figure 1c). At mantle depths (i.e., using the geophysical Moho as 4.3 km/s velocity contour), European seismic velocities are 4.4 km/s ± 0.2 km/s (Figure 2). At crustal depths, the velocity profile reaches 3.8 km/s at 20 km depth (Figure 2). Along the plunging slab, seismic velocities are lower than those in the European LC at the front of the mountain belt, that is, mostly lower than 4.0 km/s (Figure 2). At the same depth, the velocity therefore decreases from the front of the belt to the slab. Since the slab dipping is continuous (as shown in the receiver function model of Zhao et al., 2015; Figure 1a), this

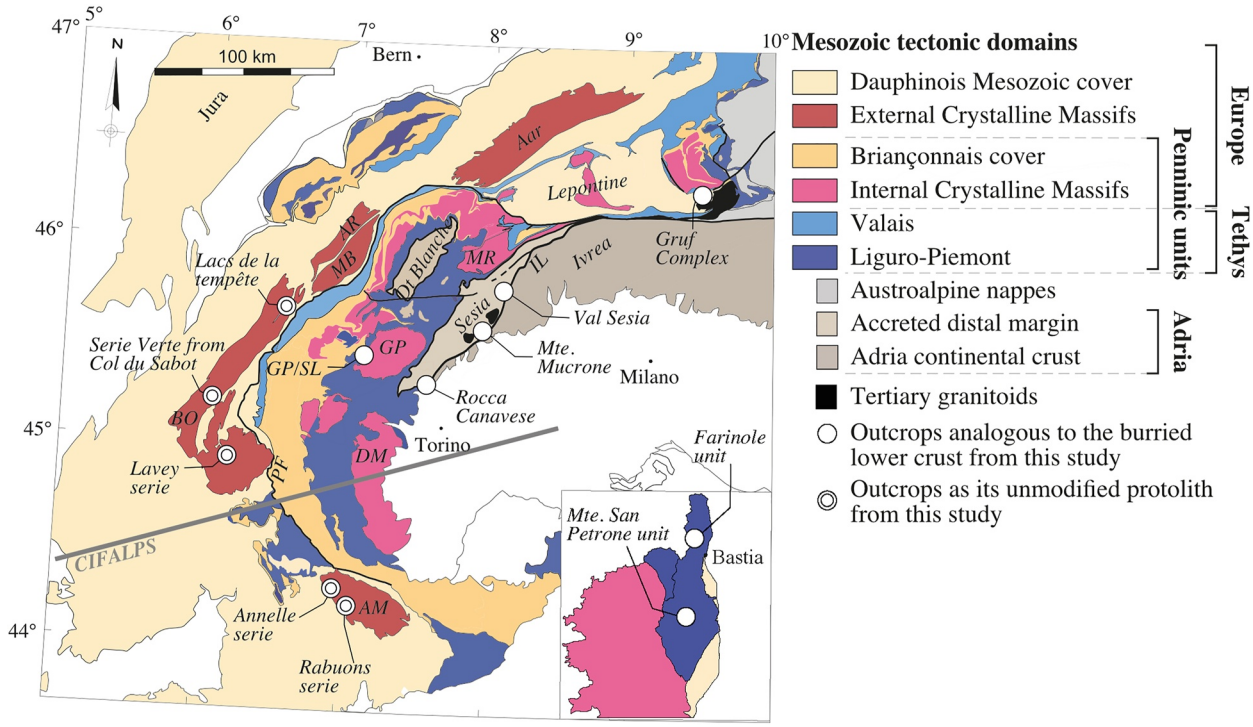

Figure 3. Location map of sample site used for modeling (geological contours after Handy & Oberhänsli, 2004; Schmid et al., 2004). Abbreviations: AM: Argentera-Mercantour; AR: Aiguilles Rouges; BO: Belledonne-Oisans; DM: Dora Maira; GP: Grand Paradiso; IL: Insubric Line; MB: Mont Blanc; MR: Monte Rosa; PF: Penninic Front; SL: Schistes Lustrés. Corsica at the same scale.

decrease is evidence of probable crustal transformations (deformation and/or metamorphism of the crust). From 20 to 50 km depth, seismic velocity increases rapidly from 3.3 to 3.9 km/s, which is beyond the resolution within the dipping slab (±0.2 km/s, Figures 1c and 2). A decrease is computed between 50 and 65 km depth, and then a second increase from 65 to 80 km appears but with a lesser confidence value (±0.4 km/s, Figures 1c and 2).

In this prospect, the European slab is finally characterized by two successive velocity steps: a well-defined first one at a shallower depth (25–45 km) and possibly a deeper and less marked one. The present study mainly focuses on the significance of the shallowest and best defined velocity step.

3. Sampling Strategy

Assuming a crustal part of the slab made of lower crustal rocks, and searching outcropping analogs, the rare field occurrences of the European LC can be classified into three different rock types. First, we sampled rocks in the external zone considered as unmodified or slightly modified basement (i.e., with no record of Alpine subduction, and therefore close to the post-variscan protolith of the European margin basement). We also sampled rocks from the internal zone, which have undergone significant burial. They represent buried metastable or reacted continental crust. Finally, we sampled rocks from the Adriatic plate, as mirror analogs of the European margin since the Adriatic LC can be considered as a remnant of the conjugate margin of the European crust (Manzotti et al., 2014). In addition to field analogs of the LC, we also sampled the rocks juxtaposed to them along supposedly deep contacts.

3.1. Basement Not Buried During the Alpine Orogeny

3.1.1. The External Crystalline Massif

The External Crystalline Massifs (ECM, Figure 3) constitute the upper to mid-crustal level of the ancient European margin (e.g., Bellahsen et al., 2012; Bellanger et al., 2015). Within these massifs, the metric-scale interbedded mafic rocks recorded high-pressure metamorphism in the Middle Carboniferous (Fréville et al., 2022). These

massifs were exhumed during the formation of the Alpine accretionary wedge (Oligo-Miocene, 34 to 5 Ma, Bellahsen et al., 2014). They constitute good analogs for the unmodified basement of the pre-Alpine European margin. The mafic intercalations sampled (Figure 3) include amphibolites and retrogressed eclogites expected to be also present in the LC.

3.1.2. The Gruf Complex

The Gruf complex is located south-east of the Lepontine Dome (Figure 3) and north of the Insubric Line (IL). It consists of migmatitic orthogneiss (including granulites), paragneiss, mica schists and associated leucogranite (Galli et al., 2011; Mintrone et al., 2022). The age of their ultra-high temperature peak is debated and could be Permian, Alpine, or both (Galli et al., 2012; Nicollet et al., 2018; Schmitz et al., 2009). These rocks constitute anyhow relics of the LC. Representative biotite orthogneiss, deformed leucogranite and charnockite of the Gruf Complex have been sampled.

3.1.3. The Adriatic Lower Crust, Ivrea Zone

The Ivrea-Verbano Zone (IVZ, Figure 3) preserves a continuous section through the Adriatic Permian lower continental crust (e.g., Boriani et al., 1990; Handy et al., 1999; Zingg et al., 1990), separated from the accreted distal Adriatic margin and Penninic domains of the Western and Central Alps by the IL. The IVZ is subdivided into two major units, the Kinzigite Formation and the Mafic Complex. The first, dominated by amphibolite- to granulite-facies metapelites (e.g., Quick et al., 2003; Redler et al., 2013), was metamorphosed during Variscan orogeny (316 ± 3 Ma, Ewing et al., 2013). The second, dominated by gabbroic, and dioritic intrusive complexes, generated a contact metamorphism affecting only the first kilometers around them (e.g., Redler et al., 2012). Sampling was carried out along the Val Sesia and Val Mastallone in both the Mafic Complex and the Kinzigite Formation. We collected metabasite, garnet-bearing metagabbro, granite, and mylonitic paragneiss.

3.2. HP Analogs

3.2.1. Monte Mucrone, Sesia Zone

The SZ is the largest exposed unit of Adriatic continental crust in the Western Alps (e.g., Compagnoni, 1977; Pognante, 1991; Roda et al., 2012; Figure 3). It is part of the distal continental margin of the Adriatic plate (e.g., Babist et al., 2006; Dal Piaz et al., 2001; Manzotti et al., 2014). The SZ is composed of three basement nappes (Gneiss Minuti Complex, Eclogitic Mica schists Complex, and II Dioritic-kinzigitic Zone) that were individualized during subduction in the Late Cretaceous (65–80 Ma) at different conditions, from 1 to 2.5 GPa and from 500 to 625°C (e.g., Roda et al., 2012). The protoliths are high-grade paragneiss equilibrated in the granulite- and amphibolite-facies and minor marbles and quartzites, intruded by Permian granitoids and gabbros (e.g., Çenki-Tok et al., 2011; Zucalli & Spalla, 2011). Metagranite, glaucophane-bearing eclogite, granodiorite and gneiss were sampled in the Monte Mucrone massif as pieces of continental crust involved in the Alpine subduction.

3.2.2. Rocca Canavese Zone

Within the SZ, the Rocca Canavese Thrust Sheet (RCT, Figure 3) is a distinct metamorphic unit located along the southern edge of the IL. It is characterized by a mélange of mantle and crustal lithologies (metapelites, metagranitoids, metabasics, and serpentinites, Roda et al., 2020). The block-in-matrix arrangement, lithological mixing, and contrasted PT-time paths suggest that mixing occurred at LP during subduction (Roda et al., 2018). The sequence sampled along the Lanzo-Canavese contact includes serpentinites, blueschist facies mylonites and biotite gneiss (Figure 3). We also sampled serpentinites as such lithology has been proposed as a component of the Alpine subduction channel (e.g., Malusà et al., 2021; Zhao et al., 2020).

3.2.3. Gran Paradiso-Schistes Lustrés Contact

Rocks along the Gran Paradiso (GP)-SL boundary were sampled as representative of the top contact of a continental crust panel. Paragneiss, orthogneiss and internal Briançonnais units make up the GP (e.g., Le Bayon & Ballevre, 2006) and form a tectonic window within the SL. The latter are composed of oceanic crustal fragments (metagabbros and metabasalts) and mantle rocks associated with marine metasediments of Jurassic to Cretaceous age (Deville, 1987). The continental units of the GP and the lower part of the SL were buried down to the eclogite facies (2.0 GPa and 500°C for the GP and 2.2 ± 0.2 GPa, 480 ± 30°C for the SL; Le Bayon & Ballevre, 2006; Plunder et al., 2012). In order to assess the signature of such a lithological contrast in seismic imaging, we sampled metabasites and mica schist from the SL and mylonitic gneiss and chlorite-bearing schist from the GP.

3.2.4. Continental Slivers From Corsica

The Alpine part of Corsica includes the SL unit, consisting of Tethyan ophiolite and metasedimentary cover rocks as well as some continent-derived slivers (e.g., Caron et al., 1979; Fournier et al., 1991), with metamorphic conditions ranging from sub-greenschist to lawsonite-eclogite facies (e.g., Vitale Brovarone et al., 2011). Several of these slivers (e.g., Farinole or San Petrone units) are interpreted as slices individualized during the Alpine convergence (e.g., Fournier et al., 1991; Jolivet et al., 1990; Lahondère et al., 1999) or as «continental extensional allochtons», related to the opening of the Tethys (Meresse et al., 2012; Vitale Brovarone et al., 2011). Relics of pre-Alpine granulite facies metamorphism are preserved in them (Martin et al., 2011). This metamorphism is interpreted as related to late Variscan extension (Vavra et al., 1999). We collected samples of kinzigites (metapelitic gneiss that underwent granulite facies metamorphism) as well as foliated and unfoliated metagabbros from the San Petrone and Farinole units (Figure 3).

4. Approach and Methods

4.1. From Bulk Chemistry to PT Velocity Map

One way to predict seismic velocity at lower crustal conditions is to consider natural rocks as isotropic and to calculate their seismic properties from the relative abundance of mineral phases using their acknowledged properties (Abers & Hacker, 2016). With single-crystal elastic parameters, the average velocities of an aggregate can be calculated for given P-T conditions using the Bina and Helffrich (1992) formalism (Hacker et al., 2003). Thus, in order to predict the evolution of the seismic properties of the rocks at equilibrium along the burial path, the bulk chemical compositions of the rocks were determined and the equilibrium paragenesis was modeled along theoretical PT trajectories for a dipping panel.

4.1.1. Bulk Chemical Composition

A subset of 48 samples was analyzed for major and minor elements (SiO_2, TiO_2, Al_2O_3, Fe_2O_{3t}, MnO, K_2O, P_2O_5, MgO, CaO, Na_2O), using the method described in Supporting Information S1. Three replicates were performed for each analysis. Blanks were analyzed to monitor instrument and digestion procedure contamination. International reference materials (ACEE, AGV-1, ATHO-1, BCR-1, BEN, BHVO-2, BIR-1, HAM, LIP-1, MAN, RGM1, UB-N) were analyzed for calibration and quality control (reproducibility and accuracy calculation). The concentration of each element was calculated as the average of 1–4 wavelengths.

4.1.2. Thermodynamic Modeling

Phase diagrams for a fixed bulk composition (i.e., pseudosections) were calculated using the Gibbs free energy minimization procedure of de Capitani and Brown (1987) with the software THERIAK/DOMINO (de Capitani and Petrakakis, 2010) and the database tcdb55cc2d.bs, mainly composed of the Holland and Powell (1998) database and its variants. The following solution models were used: chlorite (Holland et al., 1998), talc, staurolite, cordierite (Holland & Powell, 1998), white mica (Coggon & Holland, 2002), orthopyroxene (R. W. White et al., 2002), feldspar (Baldwin et al., 2005), ilmenite, garnet, biotite, spinel and liquid (R. W. White, et al., 2007), amphibole (Diener et al., 2007), omphacite, clinopyroxene (Green et al., 2007). Carpholite and olivine were considered as ideal solutions.

In order to test the impact of the variation in the number of hydroxyl bearing minerals on the seismic velocities, the saturation state of the samples was calculated over a temperature range (500–800°C at 1 GPa), using the same solution models as above, and compared to the loss on ignition (LOI) measured. Corsican kinzigite exhibits two seismic velocity jumps resulting from metamorphic reactions (Figure 5c). As explained below, one occurs along the collisional gradient, associated with the amphibolites-to-granulites transition, while the other takes place along the subduction gradient, related to eclogitization. Therefore, due to the significant potential for the reaction of this rock, this sample was chosen to assess the impact of rock hydration on seismic velocities. These were calculated in three states: undersaturated, undersaturated at lower temperatures (i.e., below 600°C) and saturated.

4.1.3. Seismic Properties Modeling Within a PT Domain

Rock seismic velocities (V_p, V_s, and V_p/Vs) within a pressure-temperature domain were calculated from single-crystal physical properties (database from Abers & Hacker, 2016). The rock mode was translated into volume percentage and mineralogical phases representing less than 1% were removed. The finite Eulerian strain

Table 1
List of Samples for Which S-Wave Velocity Has Been Calculated, Classified According to the Topology of the S-Wave Velocity Maps

Group	Rock name	Classification	Microscopic description	Location	Latitude	Longitude	Sample
1	Gruf charnockite	Felsic	Coarse grains qz (60%), pl (25%) gneiss with isolated millimeter scale bimodal gt (5%) population, surrounded by sparse chl (5%) and bt (5%) foliation	Gruf complex	46.27359	9.532712	11GR21
	Val sesia metagabbro	Mafic	Coarse grain metagabbro with px (50%), amp (15%), gt (10%), and oxides (10%) corronitic texture and minor pl (15%) matrix. Locally affected by cataclastic shear zone	Val Sesia	45.883653	8.167660	2AIV20
	Gran Paradiso gneiss	Felsic	Banded gneiss with millimeter scale qz (50%) and minor pl (15%) rich band. Wm (15%), chl (10%) and blue/green amphibole (10%). ~100 µm for the larger grain	Gran Paradiso	45.489399	7.134185	7BGP20
2	Val Sesia gneiss	Felsic	Small-grained qz (70%) ribbons with coarse pl porphyroblast (10%) and coarse-grain wm layers (20%)	Val Sesia	45.771426	8.094041	7IV20
	Canavese mylonitic blueschist	Intermediate	Gl (70%) and semi-millimetric pl porphyroblast (10%) in a chl and qz matrix with gt (10%)	Rocca Canavese	45.294805	7.566262	4ALZ20
	Argentera amphibolite	Mafic	Amp (55%) and bt (25%) coarse foliated mica schist, with qz (5%) and altered pl matrix (10%). Rare gt (<5%) and wm (<5%). Minor oxides (<5%)	Argentera series	44.40083	7.051667	AN1907
3	Corsia kinzigite	Intermediate	Banded mica schist with millimeter scale qz rich band (20%) and amp (40%), lw (20%), wm (10%) and gt (10%)	Corsica	42.358457	9.333194	3COR21
	Taou Blanc chlorito-schist	Mafic	Gt-bearing (10%) chl-schist (40%) with wm (30%) and ep (20%) layers. Grain size >200 µm	Taou Blanc massif	45.500829	7.14908	29GP20

Note. The geographic coordinate system used is WGS84. Minerals abbreviations are from Whitney and Evans (2010).

was calculated from the pressure and the material parameters by assuming the third-order finite strain equation using the Bina and Helffrich (1992) equation. Thermal expansivity, density, bulk and shear modulus were then extrapolated over a pressure range from 0.25 to 2.5 GPa and a temperature range from 100°C to 1,000°C, allowing the eventual estimates of V_p and V_s. Phases for which elastic parameters are not known were substituted by close end-members with available parameters (see Supporting Information S1 for more details). The Voigt-Reuss-Hill (VRH) arithmetic mean has been used to calculate seismic properties.

4.1.4. Seismic Properties Along PT Profiles

In this study, rock re-equilibration was modeled according to several end-member scenarios: (a) a typical Alpine subduction gradient. A constant 8°C/km gradient was chosen for representing the subduction-related PT profile based on the metamorphic records from exhumed HP-LT units in the Western Alps (Agard, 2021) and (b) a collision-related thermal gradient. We used a second order solution of the heat equation fixing surface temperature and geotherm at 25°C and 30°C/km, respectively, and the lithosphere asthenosphere boundary at a temperature of 1,300°C with an adiabatic geotherm at 0.4°C/km; (c) a collision-related thermal gradient, along which the rocks did not react and have kept a paragenesis typical of Alpine subduction. This latest case is explored to discriminate between temperature effects and mineralogy effects. PT profile calculations were performed according to the previous scenarios. For conversion of pressure to depth, we only considered lithostatic pressure along the slab and we calculated it as follows:

$$P = g * \sum_{0}^{z} \Delta z * \rho_z$$

with densities from the CIFALPS density model previously used for fitting gravity data (Zhao et al., 2015). Melts are produced in 5 lithologies (0.5 wt% in the Canavese mylonitic blueschist, 0.16 wt% in the Val Sesia metagabbro, 0.08 wt% in the Taou Blanc chlorito-schist and 0.02 wt% in the Val Sesia gneiss) along the HT profile. Although we acknowledge that the presence of melt could have a tremendous impact on effective wave velocities (Hacker et al., 2014), the present calculations are solely based on the solid rock part. The absence of present-day volcanism, the limited heat flow in the western Alps, and the age of their youngest magmatic intrusions (26–24 Ma for Novate granite, Lustrino et al., 2011) indeed point to the absence of a significant melt fraction at depth today. Moreover, a significant melt fraction would result in a significant drop in the seismic velocity, which is not observed in the profiles.

5. Results

5.1. Sample Description

A short microscopic description of the samples is given in Table 1, accompanied by microphotographs of thin sections (Figure S4 in Supporting Information S1).

5.2. Bulk Chemical Composition of Rocks and Choice of Representative Analysis

The chemical compositions of major elements were measured for 48 sampled rocks (Figure 4 and Table S1 in Supporting Information S1). The felsic

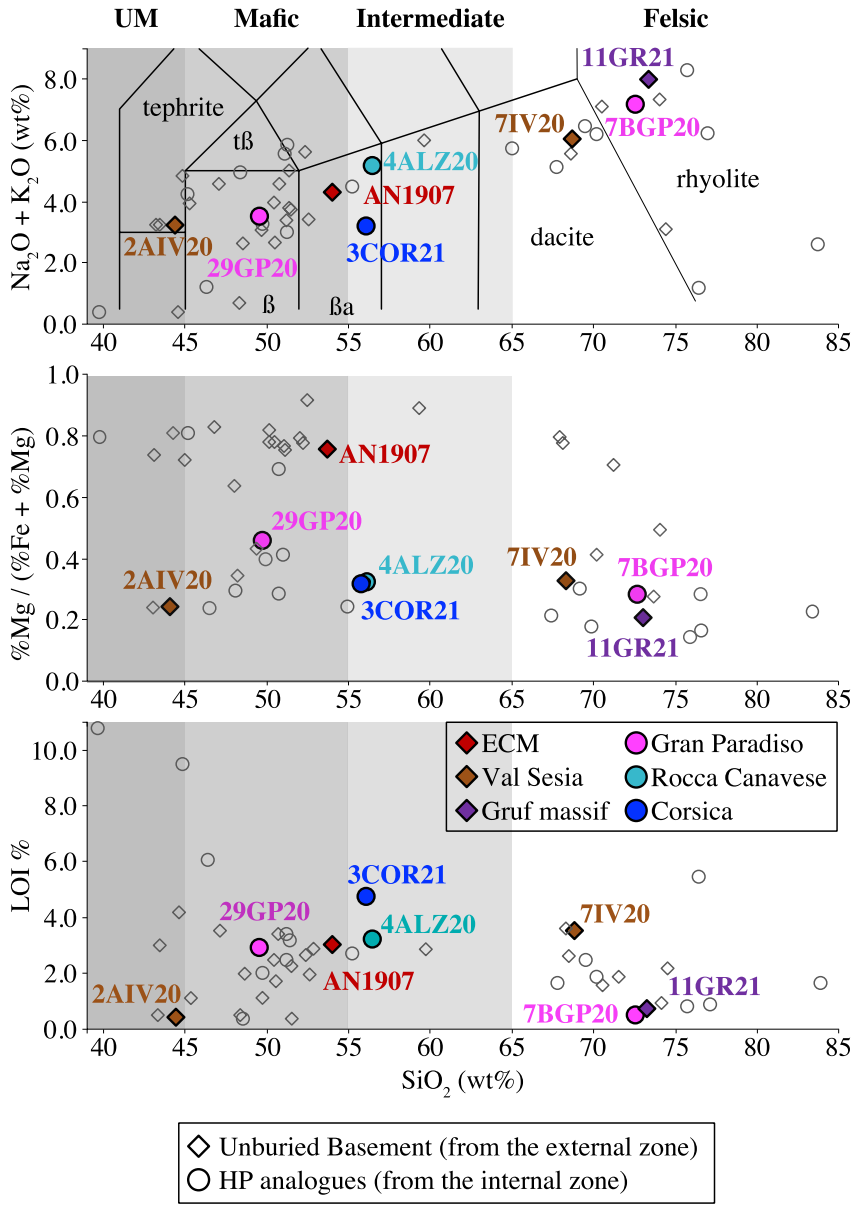

Figure 4. Chemical diagrams with locations of samples from this study. Ultra-mafic samples: SiO_2% < 45%. Mafic samples: 45 < SiO_2% < 55%. Intermediate samples: 55% < SiO_2% < 65%. Felsic samples: SiO_2% > 65%. Abbreviations: ß: basalt; ßa: basalt andesite; tß: trachy-basalt; ECM: External Crystalline Massifs. Uncertainties are smaller than the size of the circles.

composition range includes 14 samples, 5 are in the intermediate one, 22 have a mafic composition and 7 are ultramafics. Out of the 48 samples measured, 8 were chosen as representative for the chemistry range explored to compute the evolution of their seismic velocities during burial and heating.

On the alkalis sum diagram, the samples are distributed over a range from 40% to 85% SiO_2 and 0%–9% alkalis (Figure 4). Almost half of the samples lay in the basalt and its adjacent domains (trachy-basalt, tephrite and basalt andesite) with less than 6% alkalis, while the others are clustered in the dacite to rhyolite domain. Mafic rocks have a Mg# higher than 0.4, while that of felsic rocks is always below 0.4 (Figure 4). The LOI varies from 0% to 5% with a majority below 4% (Figure 4).

Of these 48 rocks, 8 samples representative of the chemical diversity were selected for velocity calculations. From the Canavese, we selected a mylonitic blueschist (4ALZ20); from the Gruf complex, a charnockite (11GR21); from GP-SL contact, a garnet-bearing gneiss (7BGP20) and from the Taou Blanc massif a chlorito-schist

10.1029/2022GC010784

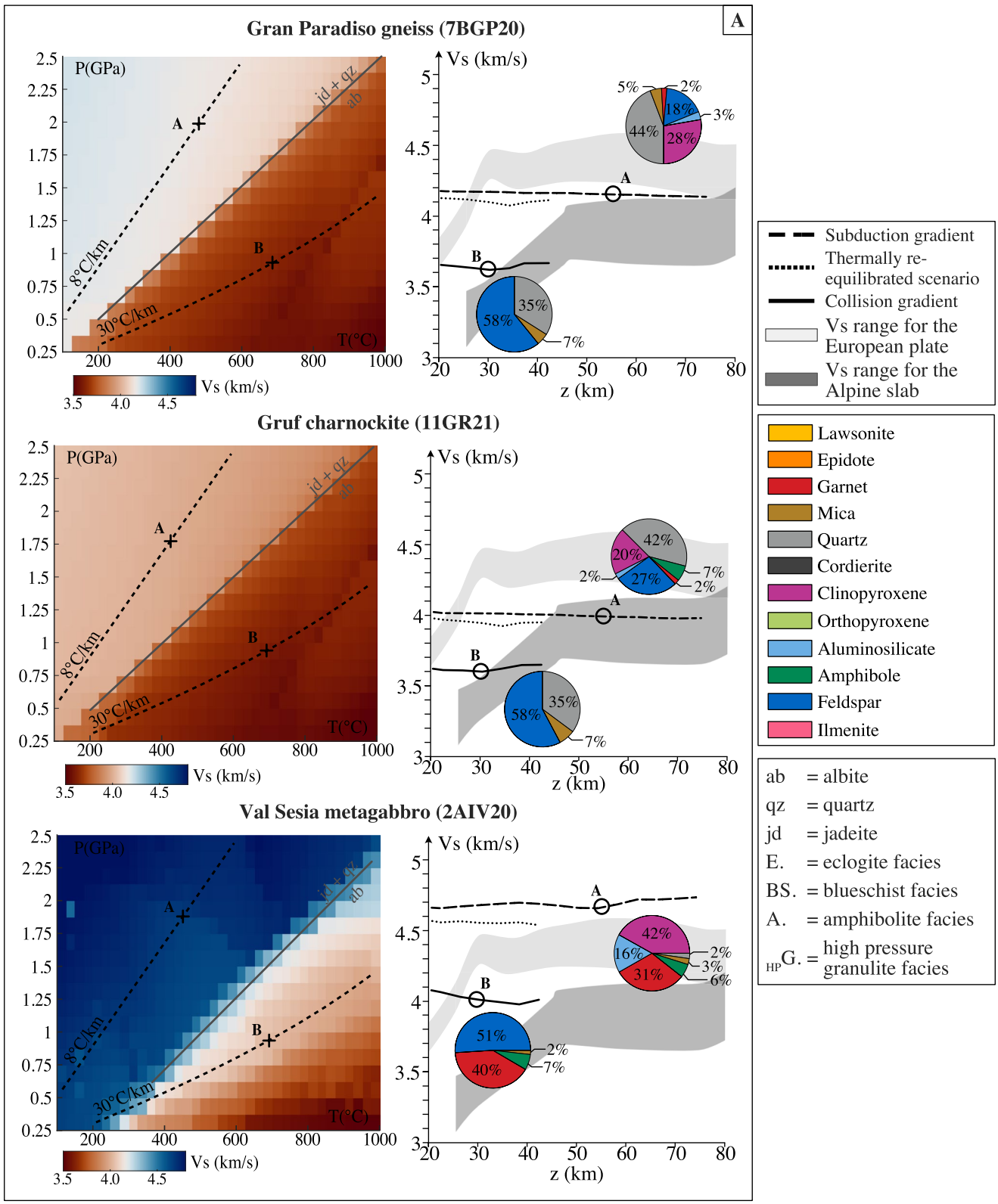

Figure 5.

(29GP20); from Val Sesia, a garnet-bearing metagabbro (2AIV20) and a gneiss of the IL (7IV20); from Monte San Petrone Unit (Corsica), a kinzigite (3COR21); from the Argentera series (ECM), an amphibolite (AN1907).

5.3. Evolution of *S*-wave Velocity Along PT Profiles

5.3.1. From Mineral Phase Maps to *S*-wave Velocity Maps

According to the topology of the obtained *S*-wave velocity maps, the samples can be classified into 3 groups (Figure 5). Indeed, instead of relying only on chemical classification, rocks have been grouped based on the visible seismic velocity fields within the studied PT range. While the rock chemical composition influences seismic field mapping by governing mineralogical assemblages, these groups are not chemically homogeneous. For instance, as shown below, group 1 is composed of two felsic samples and one ultra-mafic sample. What unites them is their limited potential for reactions. Therefore, while it is related to its chemical composition, the rock's capacity to react, "its fertility", appears to be a more relevant factor to consider. The first group includes samples for which seismic velocities are mainly governed by the plagioclase breakdown to pyroxene reaction (Figure 5a), which is known to induce a sharp impedance jump in the continental crust (Diaferia & Cammarano, 2017). The second group corresponds to samples whose velocity maps highlight the transition from amphibolites- to the HP granulites-facies (Figure 5b). The last group is made of samples whose velocity maps emphasizes the blueschist to the eclogite facies transition in addition to the amphibolites- to the HP-granulites facies transition (Figure 5c).

The first group governed by the plagioclase out joint includes 3 samples: the GP gneiss, the Gruf charnockite and the Val Sesia metagabbro. The Ab = Jd + Qz boundary limits two domains with V_s = 3.50 or 3.60 km/s and V_s = 4.00 or 4.50 km/s (Figure 5a). This boundary corresponds to a change from a plagioclase-dominated paragenesis with minor quartz at low pressure to quartz—jadeite dominated association at high pressure for the GP gneiss and the Gruf charnockite. Garnet and kyanite in a significant proportion are only computed for the Val Sesia metagabbro (Figure 5a). Thus, although their velocity topology is the same, velocity ranges differ from low values (from 3.6 to 4 km/s) for the most felsic lithology (the Gruf charnockite) to higher values (from 4 to 4.5 km/s) for the most mafic lithology (the Val Sesia metagabbro). This trend is not new. Lloyd et al. (2011) states: "According to recent compilations (e.g., Rudnick & Fountain, 1995; Rudnick & Gao, 2003), increasing average *P*-wave seismic velocities with depth indicates increasing proportions of mafic lithologies." This paper also explains how the presence of felsic rocks is necessary to match the *P*-wave velocities of the average middle crust, as a mixture of mafic rocks would generate excessively high velocities (e.g., Rudnick & Fountain, 1995; Rudnick & Gao, 2003).

The second group, governed by the amphibolites- to granulites-facies transition, consists of 3 samples: the Canavese mylonitic blueschist, the Val Sesia gneiss and the Argentera amphibolite. HP granulites- and amphibolites-facies and the Jd + Qz field are systematically delineated in the seismic velocity map of these samples (Figure 5b). The transition from amphibolites- to HP granulite facies is manifested by a mean velocity jump of 0.40 km/s (mainly from 3.60 or 3.80 km/s to 4.20 or 4.40 km/s, Figure 5b), explained by the changes from low nominal velocity minerals (plagioclase, amphibole and mica, Abers & Hacker, 2016) at LP/HT, to high nominal velocity minerals (garnet, kyanite, and pyroxene, Abers & Hacker, 2016) at HP/HT (Figure 5b).

The last group exhibits both the amphibolites- to granulites-facies and blueschist- to eclogite-facies transitions. It consists of two samples: the Taou Blanc chlorito-schist and the Corsica kinzigite (Figure 5c). The amphibolites- to granulites-facies transition appears similar to group 2 as expected. The eclogitization is shown by a velocity increase of 0.3 km/s for the kinzigite and 0.1 km/s for the chlorito-schist at 65 km depth. The velocity increase in the last sample is very small for eclogitization as along this cold subduction gradient, the eclogite facies is not completely reached. According to the seismic velocity map, a full eclogitization would generate a velocity variation of around 0.4 km/s. This increase is explained by the growth of high nominal velocity minerals (such as garnet, pyroxene, Abers & Hacker, 2016), even though low nominal velocity minerals appears (lawsonite e.g., Abers & Hacker, 2016).

Figure 5. *S*-wave velocities maps of eight rocks and their evolution along the subduction (8°C/km) and collision (30°C/km) gradient, compared to the V_s range of the Alpine slab and the one of the European plates. Samples are divided into three groups according to the topology of their seismic properties. (a) group 1: governed by the plagioclase-out reaction; (b) Group 2: one velocity jump due to the amphibolites- to granulites-facies transition; (c) Group 3: two velocity steps due to the amphibolites-granulites transition and to the eclogite-in reactions. *S*-wave velocity maps are calculated from the aggregate mode (derived from thermodynamic models, and from thermoelastic parameters) using the Hacker and Abers (2004) seismic property model. Only the phases representing more than 1% of the rock are considered in the calculation.

10.1029/2022GC010784

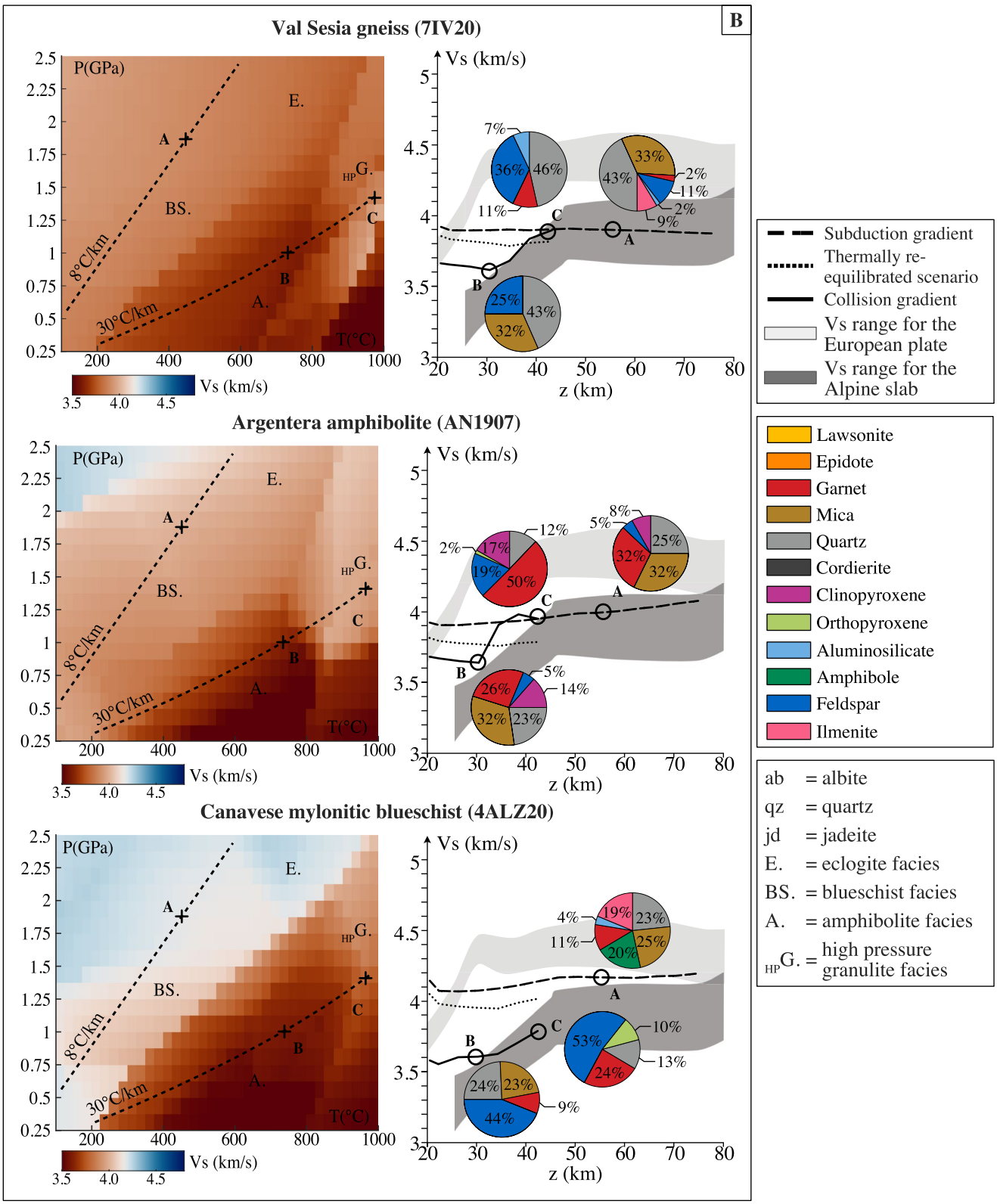

Figure 5. (Continued)

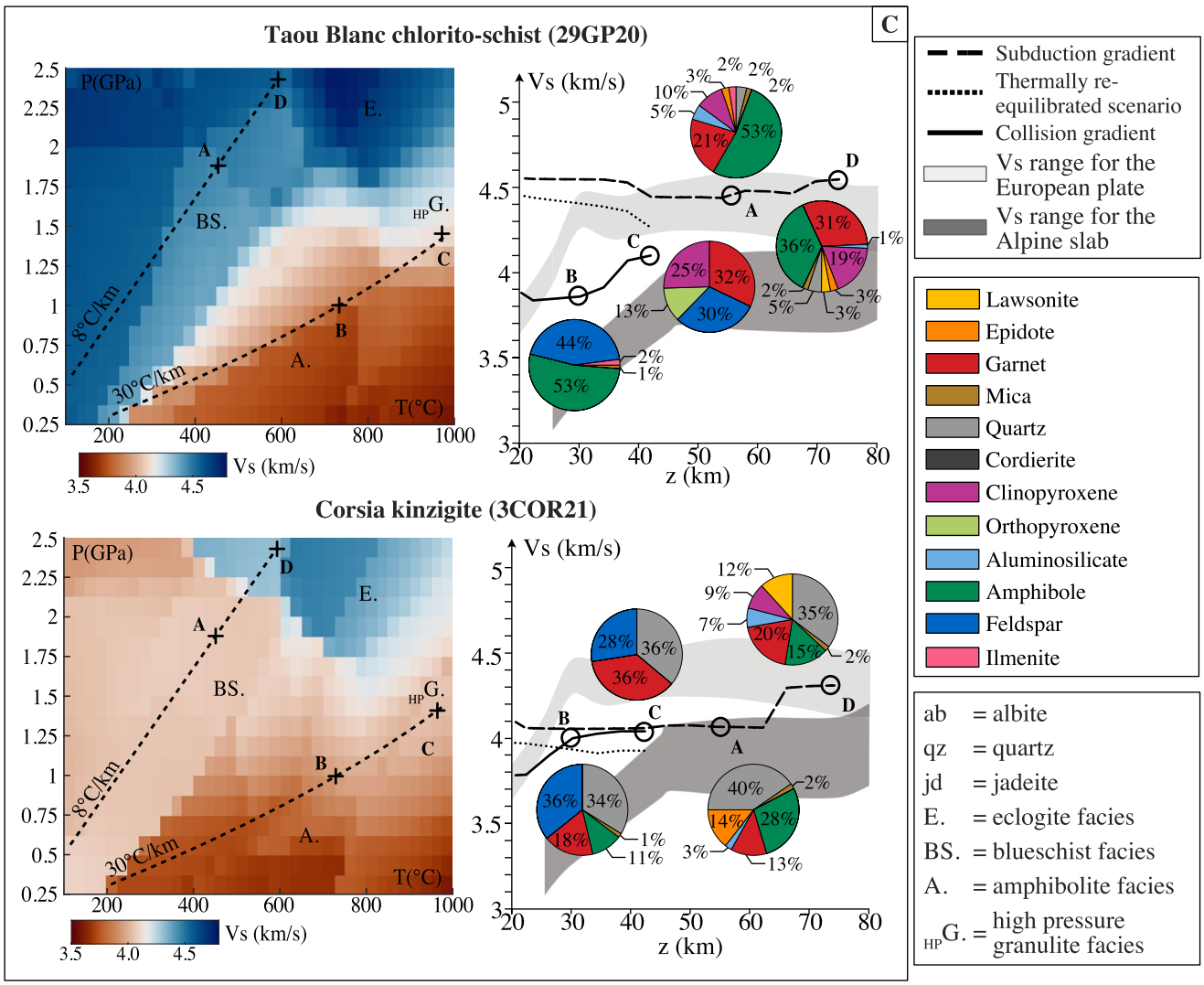

Figure 5. (Continued)

5.3.2. *S*-Wave Velocity Along Subduction or Collision PT Profile

Samples from group 2 (i.e., those highlighting only the amphibolites- to granulites-facies transition) show nearly constant velocities along the subduction gradient, reflecting minor paragenesis changes as the high-velocity domain within the eclogite facies is not reached (Figure 5b), while samples from group 3, reaching the eclogite-facies, show a step of 0.20 km/s at 65 km depth (Figure 5c). Along the collisional gradient for both groups, a significant velocity increase (around 0.2–0.3 km/s) is consistently observed at comparable depths: 3.60–3.80 km/s at 35–45 km depth for the Canavese mylonitic blueschist, 3.70–3.90 km/s at 32–38 km for Val Sesia gneiss and the Argentera amphibolite for the group 2, and to 3.80–4.10 km/s at 25–32 km for the Corsica kinzigite and 3.90–4.10 km/s at 33–40 km for the Taou Blanc chlorito-schist respectively for the group 3 (Figures 5b and 5c).

5.3.3. Impact of Water Content on *S*-wave Velocity

In order to assess the impact of the hydration state of the rock on the calculated seismic velocities and since present-day LOI does not represent the hydration state of rocks at lower crustal depths, their saturation curves were calculated on a temperature range from 500 to 800°C (Figure 6). Knowing the saturation state of the rock, hydrated or dehydrated scenarios can be explored. Two situations can be considered: either rock contain more water at depth than they do after exhumation or they may have gained water during exhumation. The different hydration states considered (i.e., saturated, highly or slightly undersaturated) allow exploration of situations expected

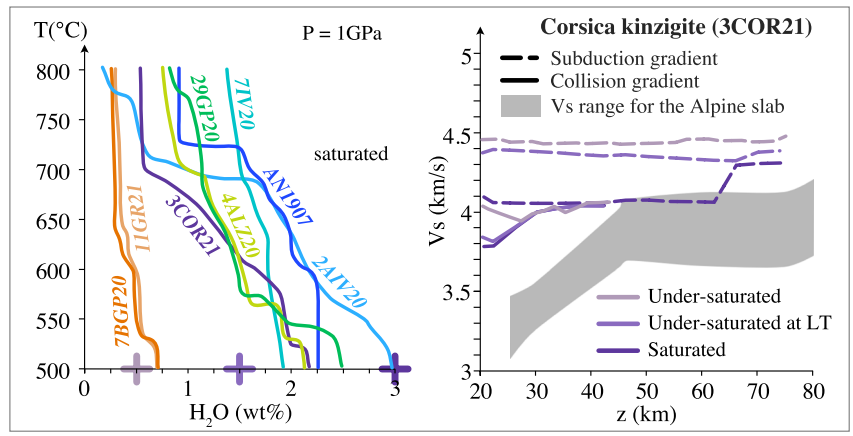

Figure 6. Saturation curves of selected samples and evolution of *S*-wave velocities of the Corsica kinzigite belonging to group 3, along the subduction (8°C/km) and collision (30°C/km) gradient, for three states of hydration, compared to the V_s range of the Alpine slab.

at lower crustal depths in a quasi-static system for 5 Ma (i.e., the end of the collision, Bellahsen et al., 2014). Depending on the initial bulk rock H_2O content, lithologies will reach their saturation curve (Figure 6) at different temperatures and hence different depths along the profile.

The stability of free water in the system was calculated for each quantity of H2O evaluated in the PT range studied. All stability limits were then plotted together to allow comparison between behaviors. The saturation thresholds vary from 0.5 to 3 wt% H_2O. The Gruf charnockite and the GP gneiss show almost constant H_2O% for saturation over the temperature range studied (Figure 6), while the Val Sesia metagabbro displays a higher variation from 3 wt% at 500°C to 0.5 wt% at 800°C (Figure 6). For the other samples, their H_2O % for saturation varies from about 2.2 wt% at 500°C to 1 wt% at 800°C (Figure 6). We chose the Corsica kinzigite as an example to evaluate the impact of H_2O content on seismic velocity as it belongs to group 3 and presents the two velocity jumps linked to the HP-granulites and eclogites facies boundaries (Figure 5c). Along the subduction gradient, a velocity increase of 0.4 km/s at 65 km depth due to eclogitization is mostly visible for the saturated state (3 wt% H_2O, Figure 6). The under-saturated evolution at lower temperature (1.5 wt% at 500°C) shows a lower velocity increase (0.1 km/s, Figure 6) some kilometers deeper. Along the collision gradient, the velocity jump is also visible in the saturated and the undersaturated evolutions at LT and its amplitude is almost 0.3 km/s at 25 km depth (Figure 6). Therefore, the velocity jumps are present only for rocks above or close to their water saturation. The amplitude of this velocity jumps increases with water saturation.

6. Discussion

6.1. Comparison Between Seismic Velocities From Geophysical Data and Calculated *S*-wave Velocities

S-wave velocities calculated from tested lithologies are compared to the range of those along the Alpine slab, as imaged along the CIFALPS transect.

6.1.1. A Poorly Reacted Felsic to Intermediate Crustal Slab Down to 70 km

Along the subduction thermal gradient, all mafic to intermediate samples yield much higher velocities than those computed along the slab (4.65 km/s for the Val Sesia metagabbro, 4.55 km/s for Taou Blanc chlorito-schist, 4.35 km/s for the Corsica kinzigite, and 4.10 km/s for Canavese mylonitic blueschist; vs. 4.00 km/s maximum in the slab, Figure 5). These velocities are closer to those of the mantle at the front of the belt (from 4.00 to 4.90 km/s, Figure 5). Along the collision thermal gradient, the *S*-wave velocities of the samples are still outside the range of those of the Alpine slab, except for the Canavese mylonitic blueschist (Figure 5b). These calculations support the idea that a fully eclogitized mafic LC panel would have the same seismic properties as the surrounding mantle (4.4 km/s at 60 km) and hence would not be distinguished from the mantle in V_s models (e.g., Christensen, 1989; Hacker & Abers, 2004; Hacker et al., 2003, 2015; Hetényi et al., 2007; Malusà et al., 2021).

By contrast, velocities of felsic samples are in the range of those of the Alpine slab: around 4.00 km/s and 3.60 km/s along the subduction and collision gradients for the Gruf charnockite and the Val Sesia gneiss (Figure 5).

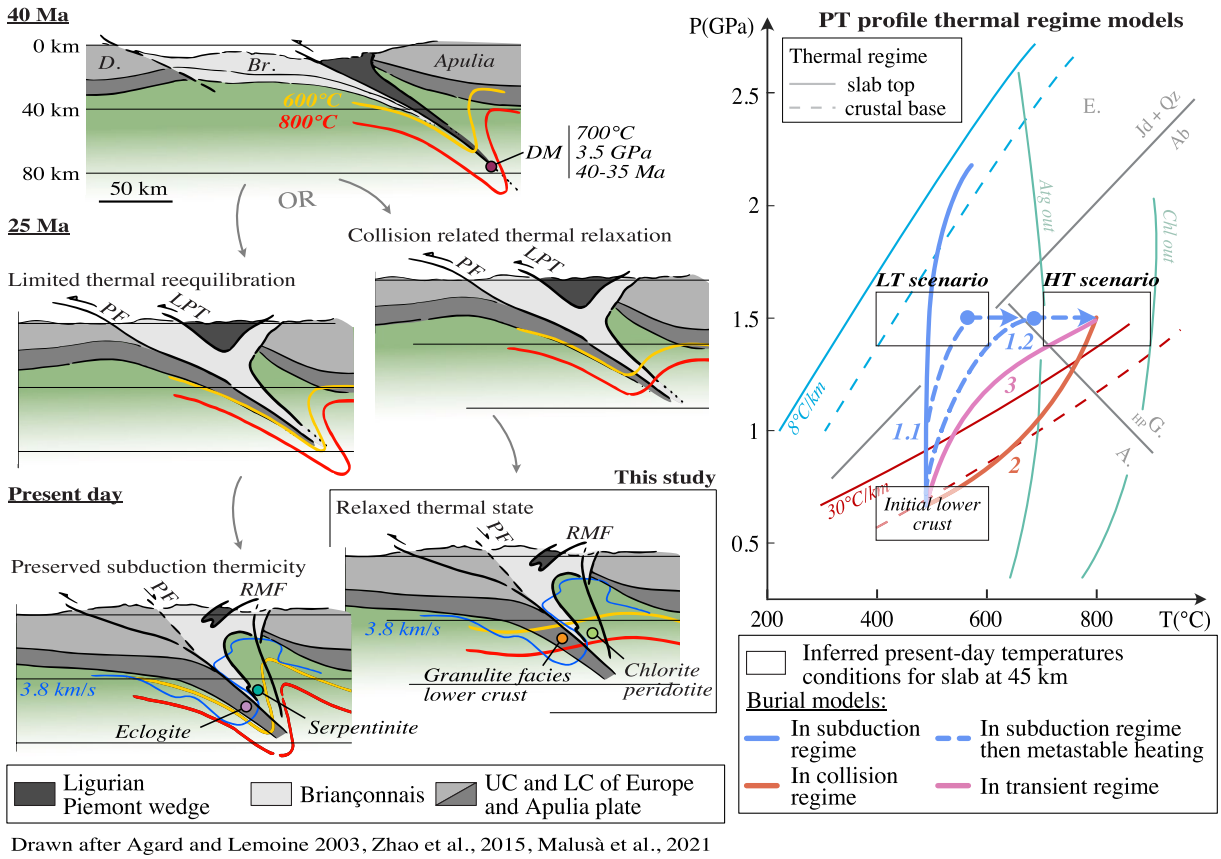

Drawn after Agard and Lemoine 2003, Zhao et al., 2015, Malusà et al., 2021

Figure 7. End-member thermal regime sketches from the continental subduction of the Alps to present-day conditions and the PT profile associated. Cross sections are at the same vertical and horizontal scales. Abbreviations: A: amphibolite facies; Br: Briançonnais; D: Dauphinois; E: Eclogites facies; $G._{HP}$: High Pressure Granulites facies; LC: lower crust; LPT: Ligurian Piemontais Thrust; PF: Penninic Front; RMF: Rivoli-Marene deep Fault; UC: upper crust. Reaction curves in green refer to the ultramafic system.

According to the V_s model, the crustal panel would have a mainly felsic to intermediate composition with only a minor or highly hydrated mafic component, as any substantial interlayering of mafic lithologies would increase the effective velocity averaged by body wave propagation (e.g., Almqvist & Mainprice, 2017; Hacker et al., 2015; Rudnick & Fountain, 1995). Of course, this conclusion highly relies on the assumption that computing rock velocities from phase proportions and absolute phase properties actually captures the natural complexity.

6.1.2. Shallow Velocity Step: The Seismic Signature of a Granulites Facies Continental Crust?

The hypothesis of an eclogitized continental crust slab top (Figure 7, model 1.1 and preserved subduction thermicity sketch) to explain the velocity increase at 25–45 km depth, implies that the slab burial path crosses the eclogite-facies boundary at low temperature. This could lead to a substantial velocity jump only for lithologies governed by the plagioclase-out reaction, that is, the first group. Since the LC was certainly already at 500–600°C before its involvement in the wedge, this hypothesis also implies an isothermal burial of the rocks (Figure 7 model 1.1). This also implies the preservation of the 8°C/km thermal gradient along the plate boundary during the involvement of the proximal European continental margin within the convergent zone and hence long after the transition from subduction and the involvement of the Briançonnais distal margin.

An alternative to the eclogitized slab top hypothesis would be a burial along a gradient modified by the introduction of the continental margin in the convergent zone (Figure 7, model 2). The end-member of this hypothesis is the burial of the continental slab along a fully reequilibrated gradient, that is, along a collision thermal gradient (Figure 7, collision related thermal relaxation sketch). In this case, lithologies belonging to the second and third groups are relevant, as they show a systematic velocity increase close to the expected depth range (Figures 5b and 5c). Whatever the privileged lithology, this scenario implies a slab reaching a temperature close to 800°C at 45 km depth.

Therefore, the two end-member scenarios mainly differ on the thermal state recorded by the continental slab at the time it was buried and since. Any intermediate scenario, with a background thermal regime warming while the continental slab is progressively involved in the subduction, would lead to an intermediate PT profile (Figure 7, model 3).

6.1.3. Seismic Signature of a Thermally Re-Equilibrated Slab

In scenarios 1.1 and 2 (Figure 7), calculations of seismic velocities consider total and instantaneous reactions at each PT condition. To test the possible effect of prograde equilibration during subduction followed by thermal re-equilibration without significant reactions (model 1.2, Figure 7), possibly due to the absence of fluids and/or strain, modes were calculated along a subduction gradient, and then seismic properties were computed with temperatures along a collision gradient to reproduce a late heated metastable slab. This approach allows us to distinguish the effect of the thermal state and that of the mineralogy alone. The evolution of seismic velocities in the only thermally re-equilibrated scenario (small dotted line Figure 5) are close to 1.1 scenario (1.2, Figure 7). This means that the effect of thermal state alone is minor, compared to the effect of mineralogy. The difference is actually lower than the uncertainty on seismic velocities and hence the difference between scenarios 1.1 and 1.2 cannot be assessed with the present data set. Derivatives of *S*-wave velocity have been published for some analogous lithologies (Zertani…). For granulites, for example, an average $\partial V/\partial V = -2.45 \times 10^{-4}$ km s^{-1} °C^{-1} and an average $\partial V/\partial P = 0.75 \times 10^{-4}$ km s^{-1} MPa have been assessed. By taking a $\Delta T = 400$°C and a $\Delta P = 1$ GPa, $\Delta V_s = -0.023$ km/s, which is well below the uncertainty in topographic seismic velocities.

6.1.4. Role of Anisotropy in Seismic Velocity Calculations

The velocity step at 45 km depth in the *S*-wave tomographic model is located in the subducted slab of the European LC at a local increase in the slab dip (Figures 1 and 2). The bending of a seismically anisotropic slab is known to induce distortion in receiver functions (e.g., Schneider et al., 2013; Shiomi & Park, 2008). In a teleseismic *P*-wave tomography model, the illumination of structures is not identical in the three directions. The present data set is based on ambient noise shear wave velocity estimates. Thus, the structures are imaged from the shear wave component of horizontally propagating Rayleigh waves. Regarding this, it is reasonable to inquire whether the velocity increase, suggested as the transition from amphibolites to granulites in the rocks, could be attributed to the influence of rock anisotropy. However, predicting the effect of rock anisotropy on apparent seismic velocities according to the wave propagation method is not straightforward. Assuming possible configurations between the wave propagation direction, the mineral fast axis direction, the arrangement of this axis within the foliation plane, and the metric to kilometric layering of the crust, and deducing the consequences on apparent velocities in geophysical data, appears to be highly exploratory.

Compared to the mantle, the sources of crustal anisotropy are numerous. In addition to rock texture, banding and layering, the presence of fractures and fissures in the middle and LC (Siegesmund et al., 1991) and fluids (Almqvist & Mainprice, 2017) are possible causes of anisotropy. Interpreting seismic anisotropy as the result of ductile deformation in the crust, leading to a strongly preferred alignment of crystallographic axes and rock texture (Almqvist & Mainprice, 2017), is therefore only possible through quantified seismic properties. The preferred crystallographic orientation (crystallographic preferred orientations (CPO)) due to the rock fluage is recognized as the main factor influencing the direction of seismic wave propagation. Consequently, many studies focus on measuring the CPO of crustal minerals. As a result, the most anisotropic crustal minerals are amphiboles and mica (e.g., Lloyd et al., 2011; Naus-Thijssen et al., 2011). According to Christensen and Mooney (1995), velocity gradients appear to result from an increase in the degree of metamorphism and a decrease in SiO_2%.

The anisotropy of felsic lithologies is therefore dominated by mica and can reach over 7% of *P*-wave or *S*-wave anisotropy (Barruol & Mainprice, 1993), although amphiboles can generate a certain degree of anisotropy (e.g., an AV_p ranging from 9.4% to 12.5% for polycrystalline glaucophanes, Park & Jung, 2022 and $AV_p \sim 38\%$ and $AV_s \sim 27\%$ for a single crystal, Bezacier et al., 2010). Llana and Brown (2012) determined by calculation and direct measurements AV_p ranging from 8.0% to 11.3% and AV_s ranging from 7.9% to 10.5% in felsic gneisses. Among the felsic lithologies studied, two (the charnockite and the gt-bearing gneiss, Figure 4) are composed of a ranging from 5% to 7% of mica and from 0% to 7% of amphiboles (Figure 5a). They also include feldspars, quartz, and clinopyroxenes (Figure 5a), which are weakly anisotropic minerals (Almqvist & Mainprice, 2017). Therefore, the expected rock anisotropy is certainly not very high. In addition, the CPO of different minerals generate destructive seismic anisotropies resulting in relatively low values for the rock. It has been shown, for example, between quartz and mica (Lamarque et al., 2016; Ward et al., 2012) or between feldspar, quartz, and pyroxene (Lamarque et al., 2016). The third felsic sample in

this study, the Sesia gneiss, is composed of 32% mica, which destabilize upon exiting the amphiboles-facies, and feldspars and quartz, whose proportions increase (Figure 5b). Unless the interplay of CPO erases the mica anisotropy, a significant anisotropy decrease is expected at the amphibolites-to-granulites transition. Erdman et al. (2013) calculated seismic properties for different metamorphic lithologies in the middle to LC of the Basin and Range. For all tested lithologies, they demonstrated that the anisotropy exhibits a slow velocity axis normal to the foliation and within the foliation plane, the properties are isotropic. Okaya et al. (2019) clarify that this conclusion cannot be generalized. If the rocks have undergone cylindrical folding, the produced anisotropy is gradually modified to the point where the distribution of structures becomes too heterogeneous for the assumption of transverse isotropy with a single axis of slow velocities to be valid in the crustal volumes. Similarly, despite the strong anisotropy conferred by planar schistosity, the variety of folds and fabric typical of phyllosilicate-rich rocks within larger-scale crustal volumes can lead to a decrease in anisotropy to the point where it may even appear isotropic (Naus-Thijssen et al., 2011). Since our samples do not exhibit cleavage or crenulation (Figure 4s), the hypothesis of a unique slow axis normal to the foliation and a decrease in anisotropy cannot be directly refuted. Thus, considering a case where the foliation plane containing the mica is horizontal and parallel to the direction of surface wave propagation, the resulting seismic recording is not affected by the vertical anisotropy of the mica. In this case, our calculated velocities are directly comparable to the ones derived from seismic data. Taking into account the effect of amphiboles, as the fast direction axis is contained in the foliation plane and parallel to the lineation, the logic is less obvious.

In contrast, the anisotropy of mafic lithologies is lower and more complex ($AV_p < 5\%$, Barruol & Mainprice, 1993 and reaching 10% AV_p in the highest anisotropy lithologies, i.e., biotite gneisses and mafic amphibolites, Barruol & Kern, 1996). HP-granulites display an $AV_p < 6\%$ and $AV_s < 4\%$, according to Llana-Fúnez and Brown (2012). Eclogites exhibit an $AV_p < 5\%$ and $AV_s < 4.5\%$ (Llana-Fúnez & Brown, 2012) or less than 3% for both *P*- and *S*-wave anisotropy (Bascou et al., 2001). If their formation is associated with ductile deformation, AV_p can reach 8% (Zertani et al., 2020). The lowest level of anisotropy is carried by the ultramafic rocks, with $AV_p \sim 2$–3% and $AV_s \sim 0.8$–1.5% (Llana-Fúnez & Brown, 2012). In eclogites and HP-granulites, the anisotropy is carried by pyroxenes (omphacite and diopside) and amphibole (Llana-Fúnez & Brown, 2012). The transition from amphiboles to granulites, which involves the destabilization of amphiboles in favor of garnets and pyroxenes, has also been quantified, resulting in a decrease in anisotropy (Brownlee et al., 2017). Among the tested lithologies, 2 samples are mafic, the Argentera amphibolite and the chlorito-schist (Figure 4). First, the amphibolites-granulites transition is expressed by a 32% loss of mica and a 5% increase in pyroxenes (Figure 5b). Although pyroxenes carry anisotropy like mica, their lower anisotropic capacity and percentage suggest a drop in anisotropy while an increase in velocity takes place. The second mafic sample, the chlorite-schist, displays a loss of 53% of amphiboles and a 38% increase in pyroxenes at the amphibolites-granulites transition (Figure 5c). Regarding the proportions of minerals involved, a lower anisotropy drop could be predicted. The velocity contrast of this sample associated with the amphibolites-granulites transition is consistent with that observed in the tomography model. A preserved anisotropy during this transformation, if it acts as a velocity decrease in the right direction, would align with those of the tomographic model.

Finally, our ultra-mafic sample, the Val Sesia metagabbro belonging to group 1, displays more than 40% of clinopyroxenes along the subduction gradient (Figure 5a) and 6% of amphiboles. Since pyroxenes are primarily responsible for the anisotropy of ultramafic rocks (Llana-Fúnez & Brown, 2012), it is possible that this sample exhibits a slight anisotropy. However, considering that the effect of anisotropy reduces the calculated seismic velocities for this sample in the right direction, its potentially weak percentage does not seem sufficient to explain the very low velocities of the Alpine slab in the tomography model.

As a result, most of the velocities calculated for the lithologies tested are slightly higher than those observed in the Alpine slab. However, the observed velocity jump is represented in the majority of lithologies and at consistent depths. In some lithologies (the Argentera amphibolite, the chlorito-schist and the Corsica kinzigite), this jump appears slightly too rapid. Since anisotropy is a factor not taken into account in our calculations, and since it allows us to lower these velocities, it is possible that these samples, containing amphibole, mica and pyroxene, are partially anisotropic. Direct measurements of seismic wave velocity and calculations of seismic properties from CPO measurements will help clarify the effect of anisotropy in our samples.

6.2. Implications for Present-Day Thermal State of the Alpine Slab

Seismic tomography in the Alps depends on the present-day thermal state of the collisional wedge, while the petrophysical properties of rocks at depth depend on the thermal state at the time they equilibrated. The heat

flow at the surface, the seismicity within the prism, and metamorphic rocks at the surface provide some information on the past and current thermal state of the orogenic prism. Heat flow maps in the Alps (e.g., Pasquale et al., 2012, 2014; Speranza et al., 2016) show values above 68 mW/m^2 at the western end of the CIFALPS profile, related to the West European Rift. In the subsiding Po plain, the heat flow drops down to 44 mW/m^2. There is thus a strong regional lateral thermal gradient at the surface with the mountain belt itself being close to the acknowledged average for the continental lithosphere (60 mW/m^2). The mantle wedge seismicity has been used to provide indirect information on the thermal state of the slab, as some earthquakes are located at the depth of the *S*-wave model velocity step in the slab (~50 km; Malusà et al., 2017). Malusà et al. (2017) inferred temperatures lower than 700°C for the mantle and hence a still cold continental slab, assuming that these earthquakes are related to the antigorite-out reaction, at 650–700°C for 2 GPa pressure (Fumagalli & Poli, 2005), in a cold and hence stiff mantle wedge. Earthquakes have nevertheless been documented at any depth in subduction mantle wedges including in hot, upper mantle beneath island arcs (L. T. White et al., 2019). Furthermore, the chlorite-out reaction occurring at 800°C for 1.5 GPa in lherzolites, that is, at 45 km depth along the slab, is a process also prone to generate earthquakes (Fumagalli & Poli, 2005). Using the same modeling approach as we used on the crustal analogs, we performed systematic calculations of V_s for a serpentinite sampled next to the blueschist mylonite from Rocca Canavese-Lanzo contact (Figure S2 in Supporting Information S1). On this pseudosection, the chlorite-out reaction generates a higher velocity contrast than the antigorite-out reaction (respectively from 4.30 to 4.60 km/s to and from 4.20 to 4.30 km/s, Figure S2 in Supporting Information S1), which is more likely to be detected by the tomographic models. Thus, the occurrence of earthquakes in the mantle wedge is not univocal evidence of a cold wedge root beneath the Alps. Chlorite-bearing peridotite units in a hot environment could have the same behavior as serpentinites in a cold setting.

Finally, numerical models (Butler et al., 2013) used as evidence for a still cold Alpine slab do not integrate the end of convergence after collision. Using an average thermal diffusivity of 1.10^{-6} m^2 s^{-1} (Gibert et al., 2003) for continental and mantle rocks at 700°C and using a scaling factor from the heat equation ($x \sim 2\sqrt{\kappa t}$), thermal re-equilibration is predicted to be achieved in 7 Myrs for a 30 km thick cold slab anomaly (Syracuse et al., 2010). Timing of significant involvement of continental units in the Alpine convergent system can be bounded by the age of HP metamorphism in the most distal continental units and the mid-Eocene age of the last deposits in the Briançonnais (Barfety et al., 1992, 1995; Jaillard, 1999), that is, 45 Ma in the Briançonnais units (Berger & Bousquet, 2008) and the age for mature collision at the Eocene-Oligocene boundary, based on the age of Barrovian metamorphic overprint in Lepontine Alps (35–28 Ma, Brouwer et al., 2005). Hence, the time span since the end of steady-state subduction thermal regime is anyhow greater than 20 Myrs. Whether the rocks now at 40 km depth only reacted when they were buried after 30 Ma or whether they also reacted during a recent thermal re-equilibration, it is highly unlikely that they developed and still preserve an HP-LT paragenesis. Eventually, magmatism documented along the IL between 33 and 30 Ma (e.g., Lustrino et al., 2011) evidenced lithospheric scale thermal relaxation at this time, possibly related to oceanic slab break-off (e.g., Rosenberg, 2004).

Therefore, these arguments do not support the idea of a present-day cold Alpine orogenic prism. Therefore, the slab velocity profile would have most probably been acquired along a partially reequilibrated thermal gradient (Figure 7, model 3). The shallow velocity step shown within the slab in the tomographic model would therefore highlight the entrance of felsic to intermediate rocks in HP granulite facies and the consumption of low seismic velocity minerals such as amphibole and/or biotite rather than the plagioclase-out reaction. This leads to the growth of mineral phases with higher seismic velocities, including garnet and pyroxene.

6.3. Possible Effects of Incomplete Reactions

As mentioned above, our calculations consider instantaneous and total reactions. Although the effects of kinetics have not been quantified in this study, it is possible to qualitatively predict its effect on seismic velocities. By considering transformations limited by reaction rates, the reaction fronts are expected to be shifted to greater depths along the slab (Hetényi et al., 2021). Rare estimates of the overstepping degree for the garnet in reaction along Barrovian gradient yield values of about 50°C and 0.2–0.5 GPa (Spear et al., 2014), hence a depth shift of about 10 ± 5 km depending on the thermal gradient. Depending on possible cascade effects, the reaction interval could also be smeared or sharpened compared to equilibrium—based modeling (Pattison et al., 2011). Thus, if the velocity jump in the tomographic model is due to metamorphic reactions, taking into account the reaction kinetics in the velocity calculation would shift the predicted velocity step to greater

depths. In this prospect, calculations from most samples (the Corsica kinzigite, the Argentera amphibolite, the Sesia gneiss, the Canavese blue-schist and the Taou Blanc chlorito-schist) yield velocity jump with amplitude similar to the observed profile but at shallower depths. On the opposite, a velocity change related to eclogitization would occur at greater depths (from 50 to 80 km). Kinetics effects could therefore explain why the amphibolites-to-granulites are imaged deeper than expected, not how the eclogite-in could occur at shallower levels.

6.4. Implications for Other Seismic Imaging Results

Among the available V_p models using local earthquake tomography, the one along the CIFALPS transect (Solarino et al., 2018) shows intriguing properties in the European LC and the dipping slab. At 30–40 km depth, from the Penninic Front (PF) to the Ivrea body, the increase in V_p from 6.70 to 7.60 km/s (Solarino et al., 2018), associated with an increase in V_s from 3.90 km/s to 4.20 km/s (Lyu et al., 2017), is interpreted as a progressive change in the metamorphic assemblage during subduction, associated with a change in density from 2.90 to 3.33 kg/m^3 (Solarino et al., 2018).

The present data set is in agreement with the results of the *P*-wave velocity model, suggesting the absence of a major inherited lithological boundary and an amphibolites-facies heritage for the European LC. V_p calculations for lithologies considered relevant for the amphibolites-to-granulites transition scenario (i.e., the Canavese mylonitic blueschist, the Val Sesia gneiss, the Argentera amphibolite) yield values between 6.8 and 7.20 km/s at 45 km depth. They are too low to explain the V_p signature at 45 km in the Alpine slab in V_p tomography images (Paul et al., 2022; Solarino et al., 2018) but could be relevant for the low velocity dipping body imaged at the top of the dipping panel ("c" domain in Solarino et al., 2018) located at the same horizontal distance to the PF Thrust as the low velocity bulge of the slab in V_s tomography. A further discussion of these apparent discrepancies is actually not possible without a consistent definition of the slab limits, which significantly vary from a model to another. A consistent inversion of V_p, V_s and their ratio, together with a depth migration of receiver functions in the same velocity model, would actually feed a further discussion of the petrological significance of velocity contrasts along the Alpine slab top.

7. Conclusion

In this paper, we calculated the seismic properties of eight crustal rocks, relevant as analogs of the lower crustal part of the Alpine slab, and compared them with the seismic profile of the Alpine slab in a recent V_s ambient noise tomography model (Nouibat et al., 2022).

The well-defined increase in velocity at 25–45 km depth in the upper part of the Alpine slab in the tomographic model can be explained by the entrance of a felsic to intermediate composition LC panel in the HP granulites facies, leading to the consumption of low nominal seismic velocity minerals, such as amphibole and/or biotite, and the growth of mineral phases with higher seismic velocities, such as garnet and pyroxene. The best felsic and intermediate analogs in the field are a kinzigite from Monte San Petrone, Corsica, a gneiss from the IL and a blueschist mylonite from the Lanzo Canavese contact. Direct measurements of seismic wave velocity and calculations of seismic properties from CPO measurements will help clarify the effect of anisotropy in our samples. No inherited lateral lithological contrast is needed to explain the velocity profile from the tomographic model. The lower level of the Variscan crust had to be still significantly hydrated to react when entering the HP granulite-facies field. This modeling implies a partially re-equilibrated thermal gradient in the Western Alps, reaching 800°C at 45 km depth, which is consistent with available evidence on the Alpine thermal state at depth. At these temperature, some chlorite-bearing ultramafics rather than serpentinites could explain the seismic signature of the slab top edge. Unless the Alpine slab hydration state is more hydrated than our field analogs, the present study implies a significant reaction overstepping for the amphibolites- to HP granulites-facies transition to be imaged at 45 km.

Data Availability Statement

All data supporting the present paper are included in the paper itself and Supporting Information S1. Data are archived at Sonnet et al. (2023).

Acknowledgments
The authors acknowledge funding through the "SYSTER" program hosted at INSU and the "RGF Alpes" project funded by the BRGM. We also thank JB Jacob for sampling in the Belledonne massif and Laurent Jolivet for the field in Corsica. We are grateful for the stimulating discussions with Claudio Rosenberg and Nicolas Bellahsen. Sascha Zertani and an anonymous reviewer are thanked for their remarks and suggestions which have greatly helped to improve this work as Claudio Faccenna for his editorial handling.

References

Abers, G. A., & Hacker, B. R. (2016). A MATLAB toolbox and Excel workbook for calculating the densities, seismic wave speeds, and major element composition of minerals and rocks at pressure and temperature. *Geochemistry, Geophysics, Geosystems*, *17*(2), 616–624. https://doi.org/10.1002/2015GC006171

Agard, P. (2021). Subduction of oceanic lithosphere in the Alps: Selective and archetypal from (slow-spreading) oceans. *Earth-Science Reviews*, *214*, 103517. https://doi.org/10.1016/j.earscirev.2021.103517

Almqvist, B. S., & Mainprice, D. (2017). Seismic properties and anisotropy of the continental crust: Predictions based on mineral texture and rock microstructure. *Reviews of Geophysics*, *55*(2), 367–433. https://doi.org/10.1002/2016RG000552

Babist, J., Handy, M. R., Konrad-Schmolke, M., & Hammerschmidt, K. (2006). Precollisional, multistage exhumation of subducted continental crust: The Sesia Zone, western Alps. *Tectonics*, *25*(6), TC6008. https://doi.org/10.1029/2005TC001927

Baldwin, J. A., Powell, R., Brown, M., Moraes, R., & Fuck, R. A. (2005). Modelling of mineral equilibria in ultrahigh-temperature metamorphic rocks from the Anápolis-Itauçu complex, central Brazil: Modelling of mineral equilibria in UHT granulites. *Journal of Metamorphic Geology*, *23*(7), 511–531. https://doi.org/10.1111/j.1525-1314.2005.00591.x

Barfety, J. C., Enay, R., & Gidon, M. (1995). L'âge des Terres Noires et des formations associées dans les environs de Grenoble. *Geologie Alpine*, *71*, 165–168.

Barfety, J. C., Tricart, P., & Jeudy de Grissac, C. (1992). La quatrième-écaille prés de Briançon (Alpes Françaises): Un olistostrome précurseur de l'orogenèse pennique éocène. *Comptes rendus de l'Académie des sciences. Série 2, Mécanique, Physique, Chimie, Sciences de l'univers, Sciences de la Terre*, *314*(1), 71–76.

Barruol, G., & Kern, H. (1996). Seismic anisotropy and shear-wave splitting in lower-crustal and upper-mantle rocks from the Ivrea zone—Experimental and calculated data. *Physics of the Earth and Planetary Interiors*, *95*(3–4), 175–194. https://doi.org/10.1016/0031-9201(95)03124-3

Barruol, G., & Mainprice, D. (1993). A quantitative evaluation of the contribution of crustal rocks to the shear wave splitting of the teleseismic SKS waves. *Physics of the Earth and Planetary Interiors*, *78*(3–4), 281–300. https://doi.org/10.1016/0031-9201(93)90161-2

Bascou, J., Barruol, G., Vauchez, A., Mainprice, D., & Egydio-Silva, M. (2001). EBSD-measured lattice-preferred orientations and seismic properties of eclogites. *Tectonophysics*, *342*(1–2), 61–80. https://doi.org/10.1016/s0040-1951(01)00156-1

Bellahsen, N., Jolivet, L., Lacombe, O., Bellanger, M., Boutoux, A., Garcia, S., et al. (2012). Mechanisms of margin inversion in the external Western Alps: Implications for crustal rheology. *Tectonophysics*, *560–561*, 62–83. https://doi.org/10.1016/j.tecto.2012.06.022

Bellahsen, N., Mouthereau, F., Boutoux, A., Bellanger, M., Lacombe, O., Jolivet, L., & Rolland, Y. (2014). Collision kinematics in the western external Alps: Kinematics of the Alpine collision. *Tectonics*, *33*(6), 1055–1088. https://doi.org/10.1002/2013TC003453

Bellanger, M., Augier, R., Bellahsen, N., Jolivet, L., Monié, P., Baudin, T., & Beyssac, O. (2015). Shortening of the European Dauphinois margin (Oisans Massif, Western Alps): New insights from RSCM maximum temperature estimates and $^{40}Ar/^{39}Ar$ in situ dating. *Journal of Geodynamics*, *83*, 37–64. https://doi.org/10.1016/j.jog.2014.09.004

Berger, A., & Bousquet, R. (2008). Subduction-related metamorphism in the Alps: Review of isotopic ages based on petrology and their geodynamic consequences. *Special Publication*, *298*(1), 117–144. https://doi.org/10.1144/SP298.7

Bezacier, L., Reynard, B., Bass, J. D., Wang, J., & Mainprice, D. (2010). Elasticity of glaucophane, seismic velocities and anisotropy of the subducted oceanic crust. *Tectonophysics*, *494*(3–4), 201–210. https://doi.org/10.1016/j.tecto.2010.09.011

Bina, C. R., & Helffrich, G. R. (1992). Calculation of elastic properties from thermodynamic equation of state principles. *Annual Review of Earth and Planetary Sciences*, *20*(1), 527–552. https://doi.org/10.1146/annurev.ea.20.050192.002523

Boriani, A., Origoni, E. G., Borghi, A., & Caironi, V. (1990). The evolution of the "Serie dei Laghi" (Strona-Ceneri and Scisti dei Laghi): The upper component of the Ivrea-Verbano crustal section; Southern Alps, North Italy and Ticino, Switzerland. *Tectonophysics*, *182*(1–2), 103–118. https://doi.org/10.1016/0040-1951(90)90345-9

Brouwer, F. M., Burri, T., Engi, M., & Berger, A. (2005). Eclogite relics in the central Alps: PT-evolution, Lu-Hf ages, and implications for formation of tectonic mélange zones. *Schweizerische Mineralogische und Petrographische Mitteilungen*, *85*(2–3), 147–174.

Brownlee, S. J., Schulte-Pelkum, V., Raju, A., Mahan, K., Condit, C., & Orlandini, O. F. (2017). Characteristics of deep crustal seismic anisotropy from a compilation of rock elasticity tensors and their expression in receiver functions. *Tectonics*, *36*(9), 1835–1857. https://doi.org/10.1002/2017tc004625

Butler, J. P., Beaumont, C., & Jamieson, R. A. (2013). The Alps 1: A working geodynamic model for burial and exhumation of (ultra)high-pressure rocks in Alpine-type orogens. *Earth and Planetary Science Letters*, *377*(378), 114–131. https://doi.org/10.1016/j.epsl.2013.06.039

Caron, J., Delcey, R., Scius, H., Eissen, J., Fraipont, P., Mawhin, B., & Reuber, I. (1979). Map distribution of the main series types in the Schistes Lustrés of Corsica. *Comptes Rendus Hebdomadaires des Seances de l'Academie des Sciences, Serie A D*, *288*(18), 1363–1366.

Çenki-Tok, B., Oliot, E., Rubatto, D., Berger, A., Engi, M., Janots, E., et al. (2011). Preservation of Permian allanite within an Alpine eclogite facies shear zone at Mt Mucrone, Italy: Mechanical and chemical behavior of allanite during mylonitization. *Lithos*, *125*(1–2), 40–50. https://doi.org/10.1016/j.lithos.2011.01.005

Chevrot, S., Villaseñor, A., Sylvander, M., Benahmed, S., Beucler, E., Cougoulat, G., et al. (2014). High-resolution imaging of the Pyrenees and Massif Central from the data of the PYROPE and IBERARRAY portable array deployments. *Journal of Geophysical Research: Solid Earth*, *119*(8), 6399–6420. https://doi.org/10.1002/2014JB010953

Christensen, N. I. (1989). Seismic velocities. In *CRC Practical handbook of physical properties of rocks and minerals* (Vol. 228).

Christensen, N. I., & Mooney, W. D. (1995). Seismic velocity structure and composition of the continental crust: A global view. *Journal of Geophysical Research*, *100*(B6), 9761–9788. https://doi.org/10.1029/95jb00259

Coggon, R., & Holland, T. J. B. (2002). Mixing properties of phengitic micas and revised garnet-phengite thermobarometers. *Journal of Metamorphic Geology*, *20*(7), 683–696. https://doi.org/10.1046/j.1525-1314.2002.00395.x

Compagnoni, R. (1977). The Sesia-Lanzo Zone: High pressure-low temperature metamorphism in the AustroAlpine continental margin. *Rendiconti Società Italiana di Mineralogia e Petrologia*, *33*(1), 335–431.

Dal Piaz, G., Cortiana, G., Del Moro, A., Martin, S., Pennacchioni, G., & Tartarotti, P. (2001). Tertiary age and paleostructural inferences of the eclogitic imprint in the Austroalpine outliers and Zermatt–Saas ophiolite, western Alps. *International Journal of Earth Sciences*, *90*(3), 668–684. https://doi.org/10.1007/s005310000177

de Capitani, C., & Brown, T. H. (1987). The computation of chemical equilibrium in complex systems containing non-ideal solutions. *Geochimica et Cosmochimica Acta*, *51*(10), 2639–2652. https://doi.org/10.1016/0016-7037(87)90145-1

de Capitani, C., & Petrakakis, K. (2010). The computation of equilibrium assemblage diagrams with Theriak/Domino software. *American Mineralogist*, *95*(7), 1006–1016. https://doi.org/10.2138/am.2010.3354

Deville, E. (1987). *Etude géologique en Vanoise orientale (Alpes occidentales françaises, Savoie): De la naissance à la structuration d'un secteur de la paléomarge européenne et de l'océan téthysien: Aspects stratigraphiques, pétrographiques et tectoniques, Travaux du Département des sciences de la terre*. Université de Savoie.

Diaferia, G., & Cammarano, F. (2017). Seismic signature of the continental crust: What thermodynamics says. An example from the Italian Peninsula. *Tectonics*, *36*(12), 3192–3208. https://doi.org/10.1002/2016TC004405

Diehl, T., Husen, S., Kissling, E., & Deichmann, N. (2009). High-resolution 3-D *P*-wave model of the Alpine crust. *Geophysical Journal International*, *179*(2), 1133–1147. https://doi.org/10.1111/j.1365-246X.2009.04331.x

Diener, J. F. A., Powell, R., White, R. W., & Holland, T. J. B. (2007). A new thermodynamic model for clino- and ortho-amphiboles in the system Na_2O–CaO–FeO–MgO–Al_2O_3–SiO_2–H_2O–O. *Journal of Metamorphic Geology*, *25*(6), 631–656. https://doi.org/10.1111/j.1525-1314.2007.00720.x

Erdman, M. E., Hacker, B. R., Zandt, G., & Seward, G. (2013). Seismic anisotropy of the crust: Electron-backscatter diffraction measurements from the Basin and range. *Geophysical Journal International*, *195*(2), 1211–1229. https://doi.org/10.1093/gji/ggt287

Ewing, T. A., Hermann, J., & Rubatto, D. (2013). The robustness of the Zr-in-rutile and Ti-in-zircon thermometers during high-temperature metamorphism (Ivrea-Verbano Zone, northern Italy). *Contributions to Mineralogy and Petrology*, *165*(4), 757–779. https://doi.org/10.1007/s00410-012-0834-5

Fournier, M., Jolivet, L., Goffé, B., & Dubois, R. (1991). Alpine Corsica metamorphic core complex. *Tectonics*, *10*(6), 1173–1186. https://doi.org/10.1029/91TC00894

Fréville, K., Trap, P., Vanardois, J., Melleton, J., Faure, M., Bruguier, O., et al. (2022). Carboniferous-Permian tectono-metamorphic evolution of the Pelvoux massif (external crystalline massif, western Alps), with discussion on flow kinematics of the Eastern-Variscan shear zone. *Bulletin de la Société Géologique de France*, *193*, 13. https://doi.org/10.1051/bsgf/2022008

Fumagalli, P., & Poli, S. (2005). Experimentally determined phase relations in hydrous peridotites to 6· 5 GPa and their consequences on the dynamics of subduction zones. *Journal of Petrology*, *46*(3), 555–578. https://doi.org/10.1093/petrology/egh088

Galli, A., Le Bayon, B., Schmidt, M. W., Burg, J.-P., Caddick, M. J., & Reusser, E. (2011). Granulites and charnockites of the Gruf complex: Evidence for Permian ultra-high temperature metamorphism in the Central Alps. *Lithos*, *124*(1–2), 17–45. https://doi.org/10.1016/j.lithos.2010.08.003

Galli, A., Le Bayon, B., Schmidt, M. W., Burg, J.-P., Reusser, E., Sergeev, S. A., & Larionov, A. (2012). U–Pb zircon dating of the Gruf complex: Disclosing the late Variscan granulitic lower crust of Europe stranded in the central Alps. *Contributions to Mineralogy and Petrology*, *163*(2), 353–378. https://doi.org/10.1007/s00410-011-0676-6

Gibert, B., Seipold, U., Tommasi, A., & Mainprice, D. (2003). Thermal diffusivity of upper mantle rocks: Influence of temperature, pressure, and the deformation fabric. *Journal of Geophysical Research*, *108*(B8), 2359. https://doi.org/10.1029/2002JB002108

Green, E., Holland, T., & Powell, R. (2007). An order-disorder model for omphacitic pyroxenes in the system jadeite-diopside-hedenbergite-acmite, with applications to eclogitic rocks. *American Mineralogist*, *92*(7), 1181–1189. https://doi.org/10.2138/am.2007.2401

Hacker, B. R., & Abers, G. A. (2004). Subduction Factory 3: An Excel worksheet and macro for calculating the densities, seismic wave speeds, and H_2O contents of minerals and rocks at pressure and temperature. *Geochemistry, Geophysics, Geosystems*, *5*(1), Q01005. https://doi.org/10.1029/2003GC000614

Hacker, B. R., Abers, G. A., Peacock, S. M., & Holloway, S. D. (2003). Subduction factory 1. Theoretical mineralogy, densities, seismic wave speeds, and H_2O contents. *Journal of Geophysical Research*, *108*(B1), 1018. https://doi.org/10.1029/2001JB001129

Hacker, B. R., Kelemen, P. B., & Behn, M. D. (2015). Continental lower crust. *Annual Review of Earth and Planetary Sciences*, *43*(1), 167–205. https://doi.org/10.1146/annurev-earth-050212-124117

Hacker, B. R., Ritzwoller, M. H., & Xie, J. (2014). Partially melted, mica-bearing crust in Central Tibet. *Tectonics*, *33*(7), 1408–1424. https://doi.org/10.1002/2014TC003545

Handy, M. R., Franz, L., Heller, F., Janott, B., & Zurbriggen, R. (1999). Multistage accretion and exhumation of the continental crust (Ivrea crustal section, Italy and Switzerland). *Tectonics*, *18*(6), 1154–1177. https://doi.org/10.1029/1999TC900034

Handy, M. R., & Oberhänsli, R. (2004). Tectono-metamorphic age map of the Alps-A new approach.

Herviou, C., Agard, P., Plunder, A., Mendes, K., Verlaguet, A., Deldicque, D., & Cubas, N. (2022). Subducted fragments of the Liguro-Piemont Ocean, western Alps: Spatial correlations and offscraping mechanisms during subduction. *Tectonophysics*, *827*, 229267. https://doi.org/10.1016/j.tecto.2022.229267

Hetényi, G., Cattin, R., Brunet, F., Bollinger, L., Vergne, J., Nábělek, J. L., & Diament, M. (2007). Density distribution of the India plate beneath the Tibetan plateau: Geophysical and petrological constraints on the kinetics of lower-crustal eclogitization. *Earth and Planetary Science Letters*, *264*(1–2), 226–244. https://doi.org/10.1016/j.epsl.2007.09.036

Hetényi, G., Chanard, K., Baumgartner, L. P., & Herman, F. (2021). Metamorphic transformation rate over large spatial and temporal scales constrained by geophysical data and coupled modelling. *Journal of Metamorphic Geology*, *39*(9), 1131–1143. https://doi.org/10.1111/jmg.12604

Hetényi, G., Molinari, I., Clinton, J., Bokelmann, G., Bondár, I., Crawford, W. C., et al. (2018). The AlpArray seismic network: A large-scale European experiment to image the Alpine Orogen. *Surveys in Geophysics*, *39*(5), 1009–1033. https://doi.org/10.1007/s10712-018-9472-4

Holland, T., Baker, J., & Powell, R. (1998). Mixing properties and activity-composition relationships of chlorites in the system MgO-FeO-Al_2O_3-SiO_2-H_2O. *European Journal of Mineralogy*, *10*(3), 395–406. https://doi.org/10.1127/ejm/10/3/0395

Holland, T., & Powell, R. (1998). An internally consistent thermodynamic data set for phases of petrological interest. *Journal of Metamorphic Geology*, *16*(3), 309–343. https://doi.org/10.1111/j.1525-1314.1998.00140.x

Jaillard, E. (1999). The late Cretaceous-Eocene sedimentation in the internal Brianconnais units of Vanoise (French Alps): Witnesses of early alpine movements. *Eclogae Geologicae Helvetiae*, *92*(2), 211–220.

Jolivet, L., Dubois, R., Fournier, M., Goffé, B., Michard, A., & Jourdan, C. (1990). Ductile extension in alpine Corsica. *Geology*, *18*(10), 1007–1010. https://doi.org/10.1130/0091-7613(1990)018<1007:DEIAC>2.3.CO;2

Lahondère, D., Rossi, P., & Lahondère, J. C. (1999). Structuration alpine d'une marge continentale externe: Le massif du Tenda (Haute-Corse). Implications géodynamiques au niveau de la transversale corse-Apennins. *Géologie de la France*(4), 27–44.

Lamarque, G., Bascou, J., Maurice, C., Cottin, J. Y., Riel, N., & Ménot, R. P. (2016). Microstructures, deformation mechanisms and seismic properties of a Palaeoproterozoic shear zone: The Mertz shear zone, East-Antarctica. *Tectonophysics*, *680*, 174–191. https://doi.org/10.1016/j.tecto.2016.05.011

Le Bayon, B., & Ballevre, M. (2006). Deformation history of a subducted continental crust (Gran Paradiso, western Alps): Continuing crustal shortening during exhumation. *Journal of Structural Geology*, *28*(5), 793–815. https://doi.org/10.1016/j.jsg.2006.02.009

Llana-Fúnez, S., & Brown, D. (2012). Contribution of crystallographic preferred orientation to seismic anisotropy across a surface analog of the continental Moho at Cabo Ortegal, Spain. *Bulletin*, *124*(9–10), 1495–1513. https://doi.org/10.1130/b30568.1

Lloyd, G. E., Butler, R. W. H., Casey, M., Tatham, D. J., & Mainprice, D. (2011). Constraints on the seismic properties of the middle and lower continental crust. *Science Progress*, *360*(1), 7–32. https://doi.org/10.1144/SP360.2

Lustrino, M., Duggen, S., & Rosenberg, C. L. (2011). The Central-Western Mediterranean: Anomalous igneous activity in an anomalous collisional tectonic setting. *Earth-Science Reviews*, *104*(1–3), 1–40. https://doi.org/10.1016/j.earscirev.2010.08.002

Lyu, C., Pedersen, H. A., Paul, A., Zhao, L., Solarino, S., & CIFALPS Working Group. (2017). Shear wave velocities in the upper mantle of the western Alps: New constraints using array analysis of seismic surface waves. *Geophysical Journal International*, *210*(1), 321–331. https://doi.org/10.1093/gji/ggx166

Malusà, M. G., Guillot, S., Zhao, L., Paul, A., Solarino, S., Dumont, T., et al. (2021). The deep structure of the Alps based on the CIFALPS seismic experiment: A synthesis. *Geochemistry, Geophysics, Geosystems*, *22*(3), e2020GC009466. https://doi.org/10.1029/2020GC009466

Malusà, M. G., Zhao, L., Eva, E., Solarino, S., Paul, A., Guillot, S., et al. (2017). Earthquakes in the western Alpine mantle wedge. *Gondwana Research*, *44*, 89–95. https://doi.org/10.1016/j.gr.2016.11.012

Manzotti, P., Ballèvre, M., Zucali, M., Robyr, M., & Engi, M. (2014). The tectonometamorphic evolution of the Sesia–Dent Blanche nappes (internal western Alps): Review and synthesis. *Swiss Journal of Geosciences*, *107*(2), 309–336. https://doi.org/10.1007/s00015-014-0172-x

Marchant, R. H., & Stampfli, G. M. (1997). Subduction of continental crust in the western Alps. *Tectonophysics*, *269*(3–4), 217–235. https://doi.org/10.1016/s0040-1951(96)00170-9

Martin, L. A., Rubatto, D., Brovarone, A. V., & Hermann, J. (2011). Late Eocene lawsonite-eclogite facies metasomatism of a granulite sliver associated to ophiolites in Alpine Corsica. *Lithos*, *125*(1–2), 620–640. https://doi.org/10.1016/j.lithos.2011.03.015

Meresse, F., Lagabrielle, Y., Malavieille, J., & Ildefonse, B. (2012). A fossil Ocean–continent transition of the Mesozoic Tethys preserved in the Schistes Lustrés nappe of northern Corsica. *Tectonophysics*, *579*, 4–16. https://doi.org/10.1016/j.tecto.2012.06.013

Mintrone, M., Galli, A., & Schmidt, M. W. (2022). Exhumation of a migmatitic unit through self-enhanced magmatic weakening enabled by tectonic contact metamorphism (Gruf complex, Central European Alps). *Contributions to Mineralogy and Petrology*, *177*(5), 56. https://doi.org/10.1007/s00410-022-01919-4

Nábělek, J., Hetényi, G., Vergne, J., Sapkota, S., Kafle, B., Jiang, M., et al. (2009). Underplating in the Himalaya-Tibet collision zone revealed by the Hi-CLIMB experiment. *Science*, *325*(5946), 1371–1374. https://doi.org/10.1126/science.1167719

Nábělek, J. L., Vergne, J., & Hetenyi, G. (2005). Project Hi-CLIMB: A synoptic view of the Himalayan collision zone and southern Tibet. In *AGU fall meeting abstracts* (Vol. 2005, p. T52A-02).

Naus-Thijssen, F. M., Goupee, A. J., Vel, S. S., & Johnson, S. E. (2011). The influence of microstructure on seismic wave speed anisotropy in the crust: Computational analysis of quartz-muscovite rocks. *Geophysical Journal International*, *185*(2), 609–621. https://doi.org/10.1111/j.1365-246x.2011.04978.x

Nicollet, C., Bosse, V., Spalla, M. I., & Schiavi, F. (2018). Eocene ultra-high temperature (UHT) metamorphism in the Gruf complex (central Alps): Constraints by LA-ICPMS zircon and monazite dating in petrographic context. *Journal of the Geological Society*, *175*(5), 774–787. https://doi.org/10.1144/jgs2018-017

Nouibat, A., Stehly, L., Paul, A., Schwartz, S., Bodin, T., Dumont, T., et al. (2022). Cifalps Team and AlpArray working Group, lithospheric transdimensional ambient-noise tomography of W-Europe: Implications for crustal-scale geometry of the W-Alps. *Geophysical Journal International*, *229*(2), 862–879. https://doi.org/10.1093/gji/ggab520

Okaya, D., Vel, S. S., Song, W. J., & Johnson, S. E. (2019). Modification of crustal seismic anisotropy by geological structures ("structural geometric anisotropy"). *Geosphere*, *15*(1), 146–170. https://doi.org/10.1130/ges01655.1

Park, Y., & Jung, H. (2022). Seismic velocity and anisotropy of glaucophane and epidote in experimentally deformed epidote blueschist and implications for seismic properties in warm subduction zones. *Earth and Planetary Science Letters*, *598*, 117822. https://doi.org/10.1016/j.epsl.2022.117822

Pasquale, V., Chiozzi, P., Verdoya, M., & Gola, G. (2012). Heat flow in the western Po Basin and the surrounding orogenic belts: Heat flow in the western Po basin. *Geophysical Journal International*, *190*(1), 8–22. https://doi.org/10.1111/j.1365-246X.2012.05486.x

Pasquale, V., Verdoya, M., & Chiozzi, P. (2014). Heat flow and geothermal resources in northern Italy. *Renewable and Sustainable Energy Reviews*, *36*, 277–285. https://doi.org/10.1016/j.rser.2014.04.075

Pattison, D. R., De Capitani, C., & Gaidies, F. (2011). Petrological consequences of variations in metamorphic reaction affinity. *Journal of Metamorphic Geology*, *29*(9), 953–977. https://doi.org/10.1111/j.1525-1314.2011.00950.x

Paul, A., Malusà, M. G., Solarino, S., Salimbeni, S., Eva, E., Nouibat, A., et al. (2022). Along-strike variations in the fossil subduction zone of the Western Alps revealed by the CIFALPS seismic experiments and their implications for exhumation of (ultra-) high-pressure rocks. *Earth and Planetary Science Letters*, *598*, 117843. https://doi.org/10.1016/j.epsl.2022.117843

Paul, A., Nouibat, A., Zhao, L., Solarino, S., Schwartz, S., Malusà, M., et al. (2021). Striking differences in lithospheric structure between the north-and south-western Alps: Insights from receiver functions along the cifalps profiles and a new Vs model. In *EGU general assembly conference abstracts* (p. EGU21-9391). https://doi.org/10.5194/egusphere-egu21-9391

Plunder, A., Agard, P., Dubacq, B., Chopin, C., & Bellanger, M. (2012). How continuous and precise is the record of P–T paths? Insights from combined thermobarometry and thermodynamic modelling into subduction dynamics (Schistes Lustrés, W. Alps). *Journal of Metamorphic Geology*, *30*(3), 323–346. https://doi.org/10.1111/j.1525-1314.2011.00969.x

Pognante, U. (1991). Petrological constraints on the eclogite-and blueschist facies metamorphism and P-T-t paths in the western Alps. *Journal of Metamorphic Geology*, *9*(1), 5–17. https://doi.org/10.1111/j.1525-1314.1991.tb00501.x

Quick, J. E., Sinigoi, S., Snoke, A. W., Kalakay, T. J., Mayer, A., & Peressini, G. (2003). Geologic map of the southern Ivrea-Verbano zone, northwestern Italy. https://doi.org/10.3133/i2776

Redler, C., Johnson, T. E., White, R. W., & Kunz, B. E. (2012). Phase equilibrium constraints on a deep crustal metamorphic field gradient: Metapelitic rocks from the Ivrea zone (NW Italy). *Journal of Metamorphic Geology*, *30*(3), 235–254. https://doi.org/10.1111/j.1525-1314.2011.00965.x

Redler, C., White, R. W., & Johnson, T. E. (2013). Migmatites in the Ivrea Zone (NW Italy): Constraints on partial melting and melt loss in metasedimentary rocks from Val Strona di Omegna. *Lithos*, *175–176*, 40–53. https://doi.org/10.1016/j.lithos.2013.04.019

Roda, M., De Salvo, F., Zucali, M., & Spalla, M. I. (2018). Structural and metamorphic evolution during tectonic mixing: Is the Rocca canavese Thrust Sheet (Italian western Alps) a subduction-related mélange? *IJG*, *137*(2), 311–329. https://doi.org/10.3301/IJG.2018.17

Roda, M., Spalla, M. I., & Marotta, A. M. (2012). Integration of natural data within a numerical model of ablative subduction: A possible interpretation for the Alpine dynamics of the Austroalpine crust. *Journal of Metamorphic Geology*, *30*(9), 973–996. https://doi.org/10.1111/jmg.12000

Roda, M., Zucali, M., Regorda, A., & Spalla, M. I. (2020). Formation and evolution of a subduction-related mélange: The example of the Rocca canavese Thrust Sheets (western Alps). *GSA Bulletin*, *132*(3–4), 884–896. https://doi.org/10.1130/B35213.1

Rondenay, S., Abers, G. A., & van Keken, P. E. (2008). Seismic imaging of subduction zone metamorphism. *Geology*, *36*(4), 275. https://doi.org/10.1130/G24112A.1

Rosenberg, C. L. (2004). Shear zones and magma ascent: A model based on a review of the Tertiary magmatism in the Alps. *Tectonics*, *23*(3), TC3002. https://doi.org/10.1029/2003TC001526

Rudnick, R. L., & Fountain, D. M. (1995). Nature and composition of the continental crust: A lower crustal perspective. *Reviews of Geophysics*, *33*(3), 267–309. https://doi.org/10.1029/95RG01302

Rudnick, R. L., & Gao, S. (2003). Composition of the continental crust. In *Treatise on geochemistry* (Vol. 3).

Schmid, S. M., Fügenschuh, B., Kissling, E., & Schuster, R. (2004). Tectonic map and overall architecture of the Alpine orogen. *Eclogae Geologicae Helvetiae*, *97*(1), 93–117. https://doi.org/10.1007/s00015-004-1113-x

Schmid, S. M., & Kissling, E. (2000). The arc of the western Alps in the light of geophysical data on deep crustal structure. *Tectonics*, *19*(1), 62–85. https://doi.org/10.1029/1999TC900057

Schmid, S. M., Kissling, E., Diehl, T., van Hinsbergen, D. J., & Molli, G. (2017). Ivrea mantle wedge, arc of the Western Alps, and kinematic evolution of the Alps–Apennines orogenic system. *Swiss Journal of Geosciences*, *110*(2), 581–612. https://doi.org/10.1007/s00015-016-0237-0

Schmitz, S., Möller, A., Wilke, M., Malzer, W., Kanngiesser, B., Bousquet, R., et al. (2009). Chemical U-Th-Pb dating of monazite by 3D-Micro X-ray fluorescence analysis with synchrotron radiation. *European Journal of Mineralogy*, *21*(5), 927–945. https://doi.org/10.1127/0935-1221/2009/0021-1964

Schneider, F. M., Yuan, X., Schurr, B., Mechie, J., Sippl, C., Haberland, C., et al. (2013). Seismic imaging of subducting continental lower crust beneath the Pamir. *Earth and Planetary Science Letters*, *375*, 101–112. https://doi.org/10.1016/j.epsl.2013.05.015

Schulte-Pelkum, V., Monsalve, G., Sheehan, A., Pandey, M. R., Sapkota, S., Bilham, R., & Wu, F. (2005). Imaging the Indian subcontinent beneath the Himalaya. *Nature*, *435*(7046), 1222–1225. https://doi.org/10.1038/nature03678

Shiomi, K., & Park, J. (2008). Structural features of the subducting slab beneath the Kii Peninsula, central Japan: Seismic evidence of slab segmentation, dehydration, and anisotropy. *Journal of Geophysical Research*, *113*(B10), B10318. https://doi.org/10.1029/2007jb005535

Siegesmund, S., Kern, H., & Vollbrecht, A. (1991). The effect of oriented microcracks on seismic velocities in an ultramylonite. *Tectonophysics*, *186*(3–4), 241–251. https://doi.org/10.1016/0040-1951(91)90361-u

Solarino, S., Malusà, M. G., Eva, E., Guillot, S., Paul, A., Schwartz, S., et al. (2018). Mantle wedge exhumation beneath the Dora-Maira (U) HP dome unravelled by local earthquake tomography (Western Alps). *Lithos*, *296–299*, 623–636. https://doi.org/10.1016/j.lithos.2017.11.035

Sonnet, M., Labrousse, L., Bascou, J., Plunder, A., Nouibat, A., & Paul, A. (2023). Bulk chemical composition of rock samples used to calculate their seismic velocity at lower crustal conditions [Dataset]. Zenodo. https://doi.org/10.5281/zenodo.8363118

Spear, F. S., Thomas, J. B., & Hallett, B. W. (2014). Overstepping the garnet isograd: A comparison of QuiG barometry and thermodynamic modeling. *Contributions to Mineralogy and Petrology*, *168*(3), 1059. https://doi.org/10.1007/s00410-014-1059-6

Speranza, F., Minelli, L., Pignatelli, A., & Gilardi, M. (2016). Curie temperature depths in the Alps and the Po Plain (northern Italy): Comparison with heat flow and seismic tomography data. *Journal of Geodynamics*, *98*, 19–30. https://doi.org/10.1016/j.jog.2016.03.012

Syracuse, E. M., van Keken, P. E., & Abers, G. A. (2010). The global range of subduction zone thermal models. *Physics of the Earth and Planetary Interiors*, *183*(1–2), 73–90. https://doi.org/10.1016/j.pepi.2010.02.004

Vavra, G., Schmid, R., & Gebauer, D. (1999). Internal morphology, habit and U-Th-Pb microanalysis of amphibolite-to-granulite facies zircons: Geochronology of the Ivrea zone (southern Alps). *Contributions to Mineralogy and Petrology*, *134*(4), 380–404. https://doi.org/10.1007/s004100050492

Vitale Brovarone, A., Beltrando, M., Malavieille, J., Giuntoli, F., Tondella, E., Groppo, C., et al. (2011). Inherited Ocean–Continent transition zones in deeply subducted terranes: Insights from Alpine Corsica. *Lithos*, *124*(3–4), 273–290. https://doi.org/10.1016/j.lithos.2011.02.013

Ward, D., Mahan, K., & Schulte-Pelkum, V. (2012). Roles of quartz and mica in seismic anisotropy of mylonites. *Geophysical Journal International*, *190*(2), 1123–1134. https://doi.org/10.1111/j.1365-246x.2012.05528.x

White, L. T., Rawlinson, N., Lister, G. S., Waldhauser, F., Hejrani, B., Thompson, D. A., et al. (2019). Earth's deepest earthquake swarms track fluid ascent beneath nascent arc volcanoes. *Earth and Planetary Science Letters*, *521*, 25–36. https://doi.org/10.1016/j.epsl.2019.05.048

White, R. W., Powell, R., & Clarke, G. L. (2002). The interpretation of reaction textures in Fe-rich metapelitic granulites of the Musgrave block, central Australia: Constraints from mineral equilibria calculations in the system K_2O–FeO–MgO–Al_2O_3–SiO_2–H_2O–TiO_2–Fe_2O_3. *Journal of Metamorphic Geology*, *20*(1), 41–55. https://doi.org/10.1046/j.0263-4929.2001.00349.x

White, R. W., Powell, R., & Holland, T. J. B. (2007). Progress relating to calculation of partial melting equilibria for metapelites. *Journal of Metamorphic Geology*, *25*(5), 511–527. https://doi.org/10.1111/j.1525-1314.2007.00711.x

Whitney, D. L., & Evans, B. W. (2010). Abbreviations for names of rock-forming minerals. *American Mineralogist*, *95*(1), 185–187. https://doi.org/10.2138/am.2010.3371

Zertani, S., Vrijmoed, J. C., Tilmann, F., John, T., Andersen, T. B., & Labrousse, L. (2020). P wave anisotropy caused by partial eclogitization of descending crust demonstrated by modeling effective petrophysical properties. *Geochemistry, Geophysics, Geosystems*, *21*(6), e2019GC008906. https://doi.org/10.1029/2019gc008906

Zhang, Z., Wang, Y., Houseman, G. A., Xu, T., Wu, Z., Yuan, X., et al. (2014). The Moho beneath western Tibet: Shear zones and eclogitization in the lower crust. *Earth and Planetary Science Letters*, *408*, 370–377. https://doi.org/10.1016/j.epsl.2014.10.022

Zhao, L., Malusà, M. G., Yuan, H., Paul, A., Guillot, S., Lu, Y., et al. (2020). Evidence for a serpentinized plate interface favouring continental subduction. *Nature Communications*, *11*(1), 2171. https://doi.org/10.1038/s41467-020-15904-7

Zhao, L., Paul, A., Guillot, S., Solarino, S., Malusà, M. G., Zheng, T., et al. (2015). First seismic evidence for continental subduction beneath the Western Alps. *Geology*, *43*(9), 815–818. https://doi.org/10.1130/G36833.1

Zingg, A., Handy, M. R., Hunziker, J. C., & Schmid, S. M. (1990). Tectonometamorphic history of the Ivrea zone and its relationship to the crustal evolution of the southern Alps. *Tectonophysics*, *182*(1–2), 169–192. https://doi.org/10.1016/0040-1951(90)90349-D

Zucalli, M., & Spalla, M. I. (2011). Prograde lawsonite during the flow of continental crust in the Alpine subduction: Strain vs. metamorphism partitioning, a field-analysis approach to infer tectonometamorphic evolutions (Sesia-Lanzo Zone, Western Italian Alps). *Journal of Structural Geology*, *33*(3), 381–398. https://doi.org/10.1016/j.jsg.2010.12.006

References From the Supporting Information

Anderson, O. L., & Isaak, D. G. (1995). Elastic constants of mantle minerals at high temperature. In T. J. Ahrens (Ed.) *Mineral physics and crystallography: A handbook of physical constants, reference shelf series* (Vol. 2, pp. 64–97). AGU.

Bass, J. D. (1995). Elasticity of minerals, glasses, and melts. In T. J. Ahrens (Ed.) *Mineral physics and crystallography: A handbook of physical constants, reference shelf series* (Vol. 2, pp. 45–63). AGU.

Berman, R. G. (1990). Mixing properties of Ca-Mg-Fe-Mn garnets. *American Mineralogist*, *75*(3–4), 328–344.

Fei, Y. (1995). Thermal expansion. In T. J. Ahrens (Ed.) *Mineral physics and crystallography: A handbook of physical constants, reference shelf series* (Vol. 2, pp. 29–44). AGU.

Holland, T. J. B., & Powell, R. (2011). An improved and extended internally consistent thermodynamic dataset for phases of petrological interest, involving a new equation of state for solids. *Journal of Metamorphic Geology*, *29*(3), 333–383. https://doi.org/10.1111/j.1525-1314.2010.00923.x

Knittle, E. (1995). Static compression measurements of equations of state. In T. J. Ahrens (Ed.) *Mineral physics and crystallography: A handbook of physical constants, reference shelf series* (Vol. 2, pp. 98–142). AGU.

Massonne, H. J. (2015). Derivation of P–T paths from high-pressure metagranites—Examples from the Gran Paradiso massif, western Alps. *Lithos*, *226*, 265–279. https://doi.org/10.1016/j.lithos.2014.12.024

Oalmann, J., Duesterhoeft, E., Möller, A., & Bousquet, R. (2019). Constraining the pressure–temperature evolution and geodynamic setting of UHT granulites and migmatitic paragneisses of the Gruf Complex, Central Alps. *International Journal of Earth Sciences*, *108*(3), 911–930. https://doi.org/10.1007/s00531-019-01686-x

Smyth, J. R., & McCormick, T. C. (1995). Crystallographic data for minerals. In *Mineral physics and crystallography: A handbook of physical constants* (Vol. 2, pp. 1–17).